國立臺灣大學電機資訊學院電子工程學研究所

碩士論文

Graduate Institute of Electronics Engineering

College of Electrical Engineering and Computer Science

National Taiwan University

Master Thesis

鐵電薄膜低溫相變及厚度效應之電性分析

Electrical Analysis of Cryogenic Phase Transition and
Thickness Effect in Ferroelectric Film

邢軼凡

Yifan Xing

指導教授：劉致為 博士

Advisor: Chee Wee Liu, Ph.D.

中華民國 112 年 7 月

July 2023

國立臺灣大學碩士學位論文
口試委員會審定書
MASTER'S THESIS ACCEPTANCE CERTIFICATE
NATIONAL TAIWAN UNIVERSITY

鐵電薄膜低溫相變及厚度效應之電性分析

Electrical Analysis of Cryogenic Phase Transition and Thickness Effect in Ferroelectric Film

本論文係 邢軼凡(學號:R10943159) 在國立臺灣大學電子工程學研究所完成之碩士學位論文,於民國 112 年 7 月 16 日承下列考試委員審查通過及口試及格,特此證明。

The undersigned, appointed by the Graduate Institute of Electronics Engineering on 16/July/2023 have examined a Master's thesis entitled above presented by Yifan Xing (student ID: R10943159) candidate and hereby certify that it is worthy of acceptance.

口試委員 Oral examination committee:

eSigned by:

07/17/2023 @ 02:25 UTC
(指導教授 Advisor)

eSigned by:
林中一
07/16/2023 @ 02:22 UTC

eSigned by:
林楚軒
07/16/2023 @ 02:15 UTC

eSigned by:
李敏鴻
07/16/2023 @ 02:01 UTC

eSigned by:
07/16/2023 @ 07:14 UTC

系主任/所長 Director: 江介宏

Related Publications (相關論文發表)

A: Journal Paper (學術期刊論文)

1. **Yifan Xing**, Yu-Rui Chen, Jer-Fu Wang, Zefu Zhao, Yun-Wen Chen, Guan-Hua Chen, Yuxuan Lin, Rachit Dobhal, and C. W. Liu, "Improved Ferroelectricity in Cryogenic Phase Transition of $Hf_{0.5}Zr_{0.5}O_2$," *IEEE Journal of the Electron Devices Society*, vol. 10, pp. 996-1002, 2022.

2. Yu-Rui Chen, Zefu Zhao, Chien-Te Tu, Yi-Chun Liu, Bo-Wei Huang, **Yifan Xing**, Guan-Hua Chen, and C. W. Liu, "I_{ON} Enhancement of $Ge_{0.98}Si_{0.02}$ Nanowire nFETs by High-κ Dielectrics," *IEEE Electron Device Letters*, vol. 43, no. 10, pp. 1601-1604, Oct. 2022.

3. Zefu Zhao, Yu-Rui Chen, Jer-Fu Wang, Yun-Wen Chen, Jia-Ren Zou, Yuxuan Lin, **Yifan Xing**, C. W. Liu, and Chenming Hu, "Engineering $Hf_{0.5}Zr_{0.5}O_2$ Ferroelectric/Antiferroelectric Phases with Oxygen Vacancy and Interface Energy Achieving High Remanent Polarization and Dielectric Constants," *IEEE Electron Device Letters*, vol. 43, no. 4, pp. 553-556, Apr. 2022.

B: Conference Paper (學術會議論文)

1. Zefu Zhao, Yu-Rui Chen, Yun-Wen Chen, Wan-Hsuan Hsieh, Jer-Fu Wang, Jia-Yang Lee, **Yifan Xing**, Guan-Hua Chen, and C. W. Liu, "Towards Epitaxial Ferroelectric HZO on n+-Si/Ge Substrates Achieving Record $2P_r = 84$ μC/cm^2 and Endurance > 1E11," *Symposium on VLSI Technology and Circuits (VLSI), 2023*.

2. Yu-Rui Chen, Yi-Chun Liu, Zefu Zhao, Wan-Hsuan Hsieh, Jia-Yang Lee, Chien-Te Tu, Bo-Wei Huang, Jer-Fu Wang, Shee-Jier Chueh, **Yifan Xing**, Guan-Hua Chen, Hung-Chun Chou, Dong Soo Woo, M. H. Lee, and C. W. Liu, "First Stacked Nanosheet FeFET Featuring Memory Window of 1.8V at Record Low Write Voltage of 2V and Endurance >1E11 Cycles," *Symposium on VLSI Technology and Circuits (VLSI), 2023*.

3. Guan-Hua Chen, **Yifan Xing**, Yu-Rui Chen, Zefu Zhao, Yun-Wen Chen, and C. W. Liu, "$Hf_{0.5}Zr_{0.5}O_2$ Orthorhombic Phase Formation by Temperature Optimization," *3rd Symposium on Nano-Device Circuits and Technologies (SNDCT), 2022*.

4. Yu-Rui Chen, Chien-Te Tu, Zefu Zhao, Yi-Chun Liu, Bo-Wei Huang, **Yifan Xing**, Guan-Hua Chen, and C. W. Liu, "Stacked Two $Ge_{0.98}Si_{0.02}$ Nanowire nFETs with High-κ Dielectrics Featuring High I_{ON} per Footprint of 4800 μA/μm at $V_{OV}=V_{DS}=0.5V$," *2023 International Symposium on VLSI Technology, Systems and Application (VLSI-TSA)*.

5. Zefu Zhao, Yu-Rui Chen, Yun-Wen Chen, **Yifan Xing**, Guan-Hua Chen, and C. W. Liu, "Engineering $Hf_{0.5}Zr_{0.5}O_2$ Ferroelectricity with Amorphous W_{OX} Bottom Electrodes Achieving High Remnant Polarization," *53rd IEEE Semiconductor Interface Specialists Conference (SISC), 2022*.

6. Yu-Rui Chen, Zefu Zhao, Yun-Wen Chen, **Yifan Xing**, Yuxuan Lin, Guan-Hua Chen, and C. W. Liu, "Optimizing Oxygen Vacancy and Interface Energy Achieving High Remnant Polarization and Dielectric Constants of Respective $Hf_{0.5}Zr_{0.5}O_2$ Superlattice and Alloy Structure," *53rd IEEE Semiconductor Interface Specialists Conference (SISC), 2022*.

7. Yun-Wen Chen, Yu-Rui Chen, Zefu Zhao, **Yifan Xing**, Guan-Hua Chen, and C. W. Liu, "Enhanced Ferroelectricity in $Hf_{0.5}Zr_{0.5}O_2$ Thin Film with Amorphous Underlayer," *53rd IEEE Semiconductor Interface Specialists Conference (SISC), 2022*.

8. Guan-Hua Chen, **Yifan Xing**, Zefu Zhao, Yu-Rui Chen, and C. W. Liu, "Identification of $Hf_{0.5}Zr_{0.5}O_2$ Orthorhombic vs Tetragonal Phase by X-Ray Absorption Spectroscopy," *NSRRC 28th Users' Meeting & Workshops, 2022*.

致謝

　　衷心感謝我的指導教授劉致為老師，您在整個研究過程中給予了我無私的指導和鼓勵。您豐富的專業知識和經驗使我能夠在研究中克服種種困難，並培養了我解決問題的能力。您不遺餘力的教學和指導讓我深刻了解到學術研究的重要性和價值，這對我意義重大。此外，您要求學生誠信、負責、合作、愛心，讓我在人格品質上也得到了成長。同時感謝口試委員林中一教授、林楚軒教授、李敏鴻教授、廖洺漢教授願意撥冗提供指導，使我的論文更加嚴謹。

　　感謝實驗室的學長姐、學弟妹們的幫助，你們的合作與交流使得我的研究更加完善，也讓我體會到了團隊合作的重要性。特別感謝 FE 組的同窗，澤夫、昱叡學長在實驗上的帶教，陳韻文博後、哲夫學長在模擬及理論上的指導，冠華、嘉洋在實驗、量測時的幫忙，宇嶸、宇聰、Rachit 一起的合作與討論，讓研究成果不斷推進。也謝謝其他組別的學長姐及同學們，你們的幫助和支持都是我完成學位不斷進步的關鍵。

　　最後謝謝我的家人與朋友們，感謝你們無條件的愛與支持，並鼓勵我堅持不懈地追求自己的夢想。

摘要

　　本篇論文討論基於氧化鉿鋯之鐵電薄膜，用於新型非揮發性記憶體。我們採用電漿輔助原子層沉積方法沉積 HfO_2-ZrO_2 混合物，並沉積 TiN 上下電極形成金屬–鐵電氧化物–金屬電容結構。電漿輔助原子層薄膜沉積的優勢在本文中討論，包括沉積溫度，前驅物，反應氣體等，以達到低缺陷沉積 $Hf_{0.5}Zr_{0.5}O_2$ 的目的。通過透射電子顯微鏡和高角度暗場技術來支援材料分析，以區分超晶格和合金結構。通過電性分析，低氧空缺含量有利於鐵電正交晶系的生成以及高氧空缺含量有利於反鐵電四方晶系的生成，本文闡明了 $Hf_{0.5}Zr_{0.5}O_2$ 的氧空缺效應。實驗介電常數是通過非滯後電容–電壓測量來提取的，以分辨晶系的含量。

　　從亞穩的四方晶系向正交晶系的低溫相變在增強所需鐵電特性中起著關鍵作用。在此研究中，我們在 $Hf_{0.5}Zr_{0.5}O_2$ 合金中實驗性地研究了低溫相變，觀察到電特性中從反鐵電向鐵電的可逆相變。我們還分析了穩定的正交晶系的形成，在超晶格 $Hf_{0.5}Zr_{0.5}O_2$ 中，77K 時具有顯著的 23%剩餘極化增加。為了驗證關於低溫下相變現象的理論，我們採用了 Landau-Ginzburg-Devonshire 理論和第一原理計算的分析組合。詳細的計算揭示了隨著溫度降低，四方晶系相對自由能增加有助於降低能量屏障，促進從亞穩的四方晶系向正交晶系的相變。這項工作提出了一個綜合的低溫相變模型，涉及 $Hf_{0.5}Zr_{0.5}O_2$ 中的四方晶系和正交晶系，為基於氧化鉿的新型低溫原件中增強鐵電性能提供了新的方法。

　　此外，通過降低 $Hf_{0.5}Zr_{0.5}O_2$ 的厚度，改善了讀出電流較低的問題。4nm 的 $Hf_{0.5}Zr_{0.5}O_2$ 的電流數量級比 6.7nm 的大 1000 倍，直流開/關比超過 10。在 1E-2 秒脈衝寬度下，4nm 的 $Hf_{0.5}Zr_{0.5}O_2$ 的交流開/關比為 2.1，並在 1E-3 秒脈衝寬度時達到飽和。

關鍵字：鐵電、反鐵電、氧空缺、超晶格、低溫相變、鐵電隨機存取記憶體、鐵電穿隧結、鐵電場效電晶體

Abstract

This dissertation investigates the HfO$_2$-ZrO$_2$-based ferroelectric thin film for novel non-volatile memory. The HfO$_2$-ZrO$_2$ mixture is deposited by plasma enhanced atomic layer deposition (PEALD) and sandwiched by in-*situ* TiN electrodes, forming the MFM capacitor structure. The advantages of PEALD thin film deposition are studied to optimize the quality of Hf$_{0.5}$Zr$_{0.5}$O$_2$. The transmission electron microscope and high-angle annular dark-field support material analysis to distinguish the superlattices and alloys. The oxygen vacancy effect of Hf$_{0.5}$Zr$_{0.5}$O$_2$ is clarified by electrical characteristics in low oxygen vacancy favoring ferroelectric orthorhombic phase and high oxygen vacancy favoring anti-ferroelectric tetragonal phase. The experimental dielectric constant is extracted from non-hysteretic capacitance-voltage measurement.

The cryogenic transition from the metastable tetragonal phase to the orthorhombic phase is crucial in achieving desired ferroelectric characteristics. In this study, we experimentally investigate the cryogenic phase transition in Hf$_{0.5}$Zr$_{0.5}$O$_2$ alloys, observing the reversible change from antiferroelectricity to ferroelectricity in electrical properties. We also analyze the formation of stabilized o-phase, which exhibits a significant 23% increase in remanent polarization at 77K in superlattice Hf$_{0.5}$Zr$_{0.5}$O$_2$. To provide theoretical insights into the phase transition phenomenon at lower temperatures, we employ a combination of Landau-Ginzburg-Devonshire theory and first-principle calculations. The detailed calculations reveal that the increasing relative free energy of the t-phase contributes to lowering the energy barrier as the temperature decreases, facilitating the transition from the metastable tetragonal phase to the orthorhombic phase. This research presents a comprehensive cryogenic phase transition model involving tetragonal and orthorhombic phases in Hf$_{0.5}$Zr$_{0.5}$O$_2$, offering a promising approach to

enhance ferroelectricity in emerging cryo-devices based on HfO_2.

Moreover, the issue of low read-out current is ameliorated by reducing the thickness of $Hf_{0.5}Zr_{0.5}O_2$. The current magnitude of 4nm $Hf_{0.5}Zr_{0.5}O_2$ is 1000 times more than 6.7nm with a DC swept on/off ratio of more than 10. The AC on/off ratio of 4nm $Hf_{0.5}Zr_{0.5}O_2$ is 2.1 at pulse width 1E-2 second and saturates at pulse width 1E-3 second.

Table of Contents

List of Figures

List of Tables

Chapter 1 - Introduction

1.1 Background and Motivation

Non-volatile memory (NVM) has attracted the excellent research interest in recent years due to its performance, scalability, density, and power efficiency[1]. The novel NVMs such as resistive RAM (ReRAM)[2], phase-change memory (PCM)[3], magnetic RAM (MRAM)[4], ferroelectric FET (FeFET)[5], and other emerging memories demonstrate excellent abilities which surpass that of the classic memories and are available from various industrial platforms (Fig. 1.1-1). As data storage requirements grow, the NVMs emphasize increasing memory density and scalability. Due to the ever-increasing need for high-performance computing (HPC), the data must be accessed quickly enough[6]. This leads to the shortened distance between memory and logic transistors. The demands of embedded memory have become necessary and drive the investigation of embedded non-volatile memory (eNVM)[7]. Taking advantage of low cost, high density, good scalability, and endurance, ferroelectric (FE) based memory becomes a big hit with the possibility of filling the gap between dynamic random-access memory (DRAM) and NAND Flash in the memory hierarchy (Fig. 1.1-2).

Due to their low operating power requirements, ferroelectrics are an ideal material choice for NVMs [8]. Within the realm of FE memory concepts, three distinct approaches can be identified: FeRAM[9] (Fig. 1.1-3 (a)), FTJ[10](Fig. 1.1-3 (b)), and FeFET[11](Fig. 1.1-3 (c)). FeRAM uses the direct measurement of the charge flowing during capacitor switching for readout. FTJ, on the other hand, the direction of the FE polarization modulates the tunneling current through either a thin FE layer or a FE layer in series with a thin tunneling barrier. Lastly, FeFET involves coupling the polarization to the channel of a FET, thereby altering the threshold voltage (V_T) of the transistor.

1

Significant advancements in ferroelectricity have emerged from doped-HfO_2 mixtures[12], opening up possibilities for emerging NVMs [13-15] that are compatible with complementary metal-oxide-semiconductor (CMOS) technology[16]. With the evolution towards cryo-CMOS and quantum systems, the demand for cryogenic NVMs becomes apparent[17]. Our recent research highlighted the application of $Hf_xZr_{1-x}O_2$ as a high-k dielectric due to its anti-ferroelectric (AFE) property[18]. A substantial proportion of the orthorhombic phase (o-phase) is required to obtain robust FE properties. Thermal processing of $Hf_xZr_{1-x}O_2$ thin films has been reported to induce the formation of the o-phase, resulting in ferroelectricity[19, 20]. The metastable o-phase has been observed during the cooling stage, where the material is heated to a high crystallization temperature and then cooled to room temperature[21]. The electrical characteristics of $Hf_xZr_{1-x}O_2$ are influenced by the presence of crystalline phases such as the dielectric (DE) monoclinic phase (m-phase), FE o-phase, and AFE tetragonal phase (t-phase)[22]. Consequently, a high concentration of [Hf] promotes the o-phase, while a high concentration of [Zr] favors the t-phase with AFE behavior. It has been demonstrated that the o-phase can be stabilized at specific thicknesses by manipulating the surface energy effect[23]. Additionally, our previous work has discussed the impact of oxygen vacancy concentration ($[V_o]$) on phase formation[24]. Control of $[V_o]$ allows us to tailor the FE and AFE characteristics of our metal-ferroelectric-metal (MFM) and metal-insulator-metal (MIM) heterostructures at room temperature. Higher $[V_o]$ leads to the formation of alloys, promoting AFE behavior, whereas lower $[V_o]$ results in superlattices favoring FE characteristics at room temperature[24]. Furthermore, the use of superlattice structures in $Hf_xZr_{1-x}O_2$ has been found to favor the o-phase, while alloys assist in forming the t-phase with a relatively high dielectric constant[24].

2
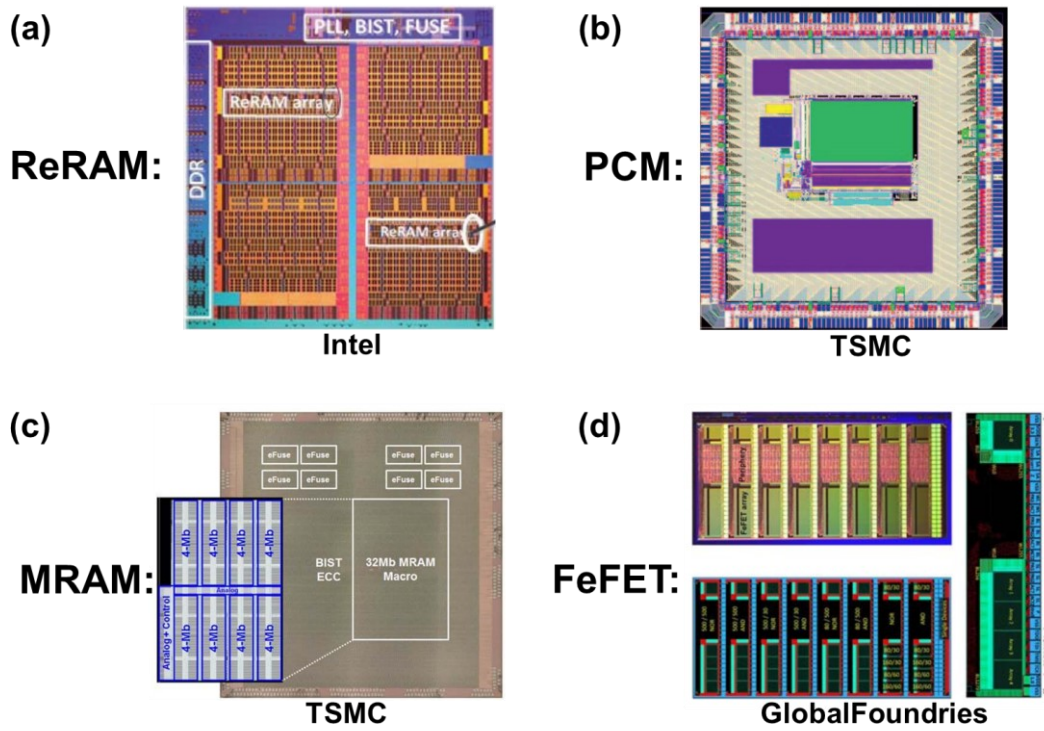
Fig. 1.1-1 Emerging memories like (a) ReRAM [2], (b) PCM [3], (c) MRAM [4], and (d) FeFET [5] are available from various industrial platforms.
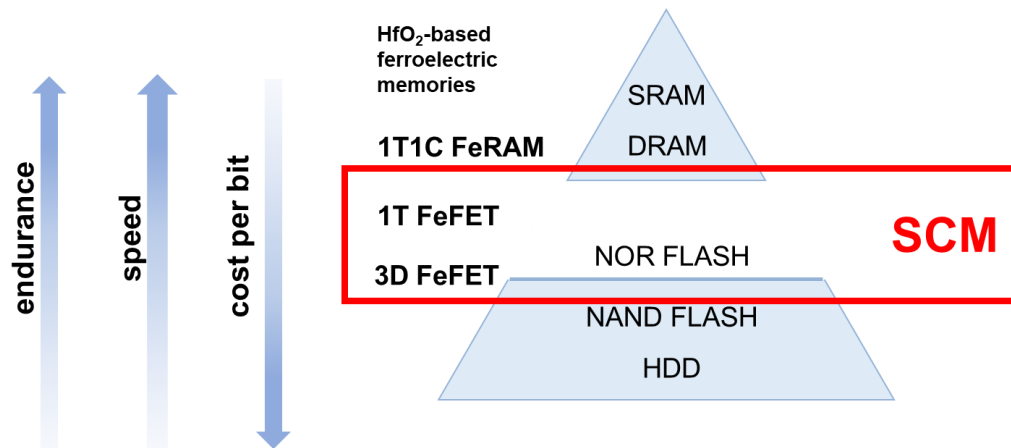
Fig. 1.1-2 Memory hierarchy.

3
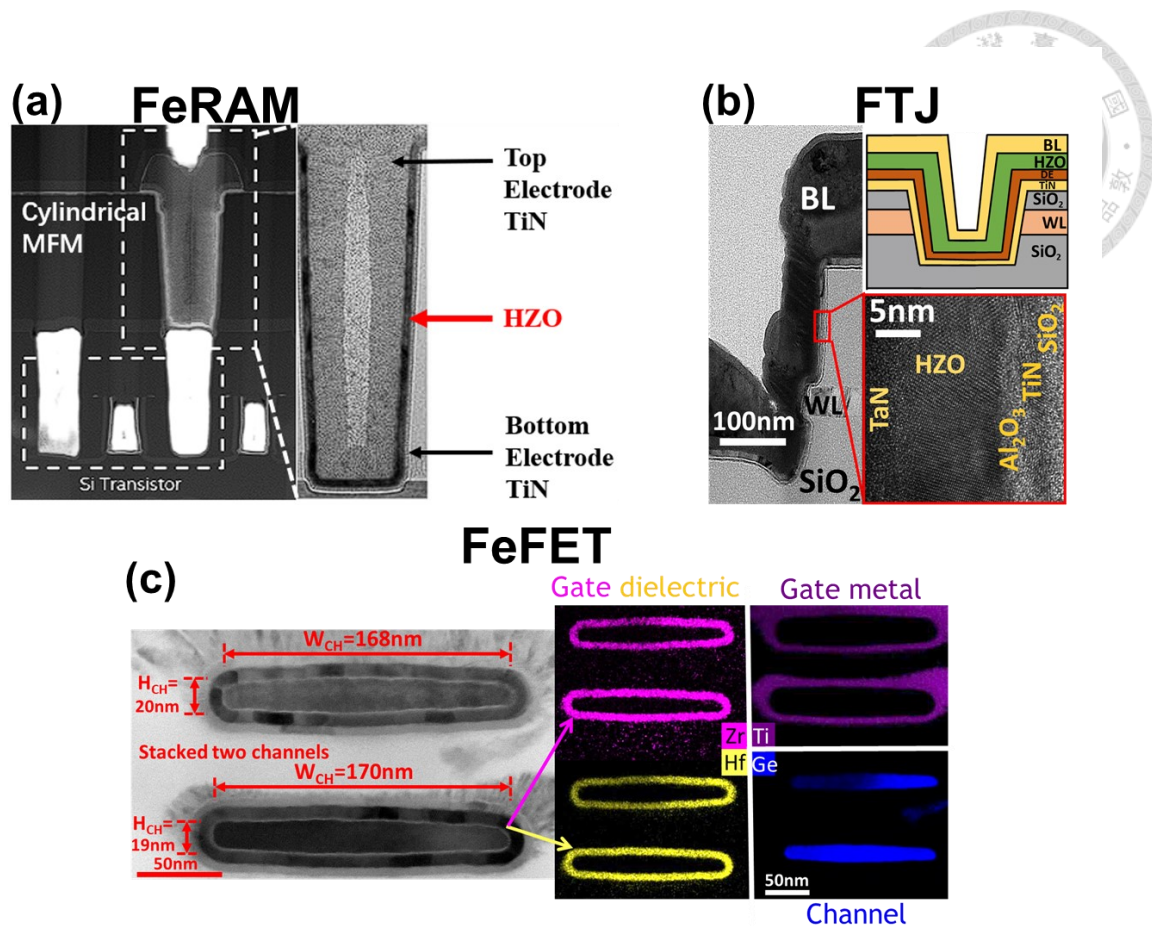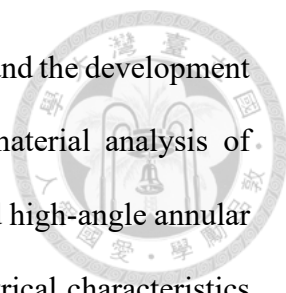
Fig. 1.1-3 Main components of ferroelectric NVMs, (a) FeRAM [9], (b) FTJ [10], and (c) FeFET [11].

1.2 Thesis Organization

The objections of this thesis are to investigate the material properties of $Hf_{0.5}Zr_{0.5}O_2$ heterostructures, $[V_o]$ effect resulting from plasma enhanced atomic layer deposition (PEALD) O_2 exposure time, and the cryogenic phase transition between FE o-phase and AFE t-phase. The thickness effect of $Hf_{0.5}Zr_{0.5}O_2$ in an MFM capacitor is also studied by measured DC/AC on/off ratio. The arrangement of this thesis is as follows.

Chapter 2 discusses the advancements in FE thin film deposition, particularly focusing on $Hf_{0.5}Zr_{0.5}O_2$ thin films deposited with TiN bottom and top electrodes. It highlights the use of atomic layer deposition (ALD) for precise control of film growth

4

and improved thin film quality. The limitations of conventional ALD and the development of PEALD are also mentioned. Chapter 2 further describes the material analysis of $Hf_{0.5}Zr_{0.5}O_2$ films using transmission electron microscopy (TEM) and high-angle annular dark-field (HAADF) imaging. It concludes with examining the electrical characteristics and dielectric constant of $Hf_{0.5}Zr_{0.5}O_2$ with different O_2 exposure times.

In Chapter 3, cryogenic behavior and phase transitions of $Hf_{0.5}Zr_{0.5}O_2$ thin films with different oxygen exposures are included. The analysis utilizes cryogenic measurements, Landau-Ginzburg-Devonshire (LGD) theory, and first-principle calculations to understand the phase transitions. The study demonstrates the reversible phase transitions between AFE and FE in $Hf_{0.5}Zr_{0.5}O_2$ thin films at cryogenic temperatures. The findings highlight the importance of temperature-dependent energy barriers and the role of different phases in controlling the FE properties of the material. These insights contribute to the understanding and potential optimization of $Hf_{0.5}Zr_{0.5}O_2$ for various applications in FE devices.

Chapter 4 shows the DC and AC on/off ratio of $Hf_{0.5}Zr_{0.5}O_2$ with 30s O_2 exposures. In the DC measurement, positive and negative voltage sweeps are applied to set the polarization direction, and the resulting on-current (J_{on}) and off-current (J_{off}) are measured. The AC measurements are performed with varying pulse widths, and the on/off ratio is analyzed. To further improve the read-out current, the thickness of $Hf_{0.5}Zr_{0.5}O_2$ is decreased. The electrical characteristics of $Hf_{0.5}Zr_{0.5}O_2$ with different thicknesses are studied and benchmarked.

Finally, chapter 5 summarizes this work's conclusions and recommends future work prospects.

Chapter 2 - Device Fabrication and Electrical Properties of Alloy and Superlattice $Hf_{0.5}Zr_{0.5}O_2$
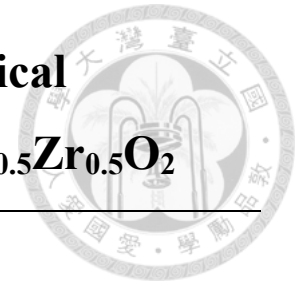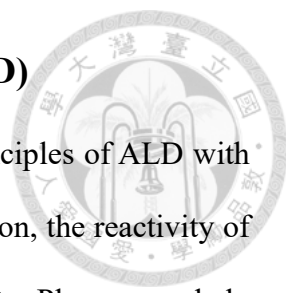
2.1 Introduction

FE thin film deposition has witnessed significant advancements in recent years, enabling the development of new materials and devices with enhanced functionalities[25]. The $Hf_xZr_{1-x}O_2$ thin film deposited with TiN bottom and top electrodes can achieve excellent FE properties due to the in-*situ* environment during whole growth flow[26]. Benefiting from the precise control of film thickness, growth temperature, and reactant gas, ALD is separately used in FE film deposition[27]. ALD offers improved reactivity of precursor molecules to achieve atomic-level control of thin film growth and high-quality thin films with reduced defect density. The MFM heterogenous is fabricated for material and electrical characteristics analysis.

However, conventional ALD faces limitations regarding certain materials and high-aspect-ratio structures. These challenges have led to the development of PEALD, which enhances the capabilities of ALD through the incorporation of plasma[28]. To measure the electrical characteristics, the bottom and top electrodes should be well defined by reactive ion etching (RIE) on the MFM structure. Metal material and etching gas need to be considered to obtain good etching selectivity. Etching time should also be well calculated according to the oxide thickness. Duo to FE properties exist in crystallized phases, post-metal annealing (PMA) or post-deposition annealing (PDA) with preferred temperature need to be performed to crystallize the $Hf_XZr_{1-X}O_2$ thin film[29].

2.2 Plasma Enhanced Atomic Layer Deposition (PEALD)

PEALD is a thin film deposition system that combines the principles of ALD with the profit of plasma. By utilizing plasma in the specific film deposition, the reactivity of precursor molecules is improved, leading to reliable thin film quality. Plasma can help break down precursor molecules more efficiently, reducing defect density. Taking advantage of film conformality, PEALD is widely applied to film formation on complex structures. Compared with the Physical vapor deposition system, PEALD enhances the diffusion of precursor molecules into narrow and high-aspect-ratio features, ensuring uniform film coverage across the substrate, including sidewalls and cavities. PEALD broadens the scope of materials that can be effectively deposited. This allows for greater flexibility in selecting materials for specific applications. Otherwise, the profit of plasma in PEALD offers the ability to tune and control the properties of the deposited films. By adjusting the plasma conditions, such as power, gas composition, pressure, and exposure time, it is possible to modify the film's crystallinity, defect density, and oxygen vacancy concentration.

Fig. 2.2-1 demonstrates the schematic of the PEALD system. The manual and ALD valves are used to control the switch and pulse precursor, respectively. Note that the heater system surrounds the chamber to maintain the growth temperature. All the unreacted precursor and by-product gas (e.g., H_2O, CO_2) are taken away by Ar purge through the pump. Besides, the dry pump system keeps the high vacuum level, benefiting the film quality.

The process of single-layer growth in PEALD is shown in Fig. 2.2-2. The relationship between pressure and time in one cycle film deposition is simplified to the waveform in Fig. 2.2-2. The precursor is pulsed after flowing Ar carrier gas and Ar purge gas, reacting with the substrate surface, which is fully covered with OH^- groups in the

7

chamber. To satisfy the formation of different films, plasma can be modified by changing

the category of reactant gas.
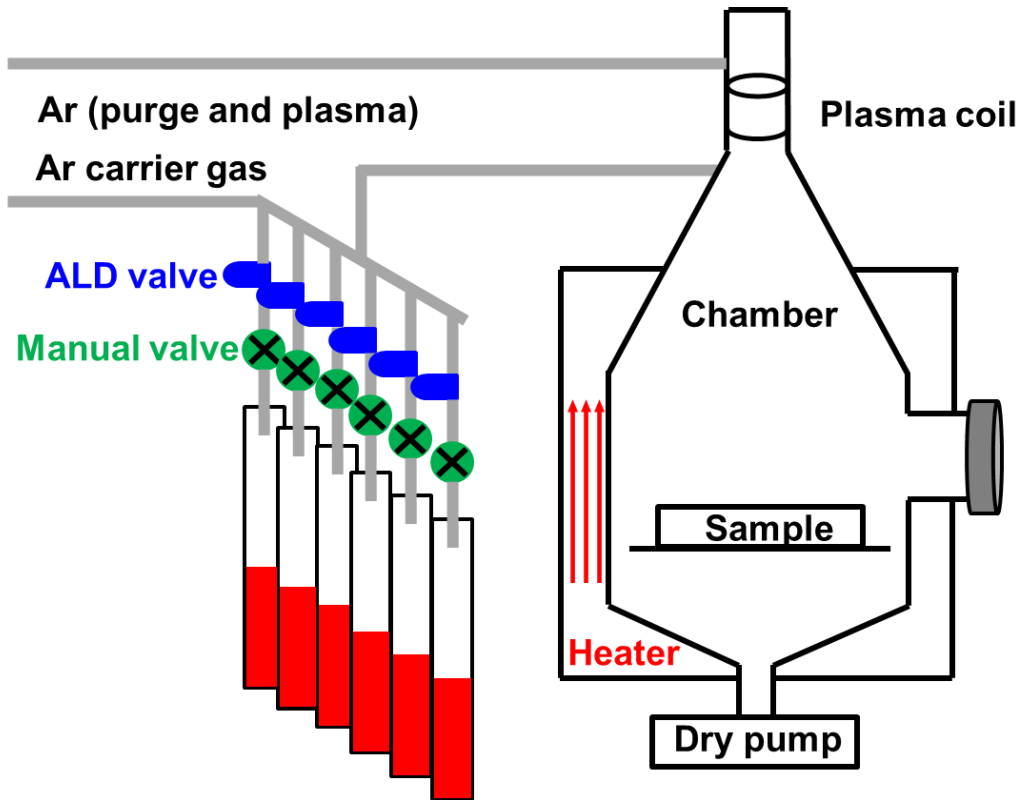
Fig. 2.2-1 Schematic of PEALD.
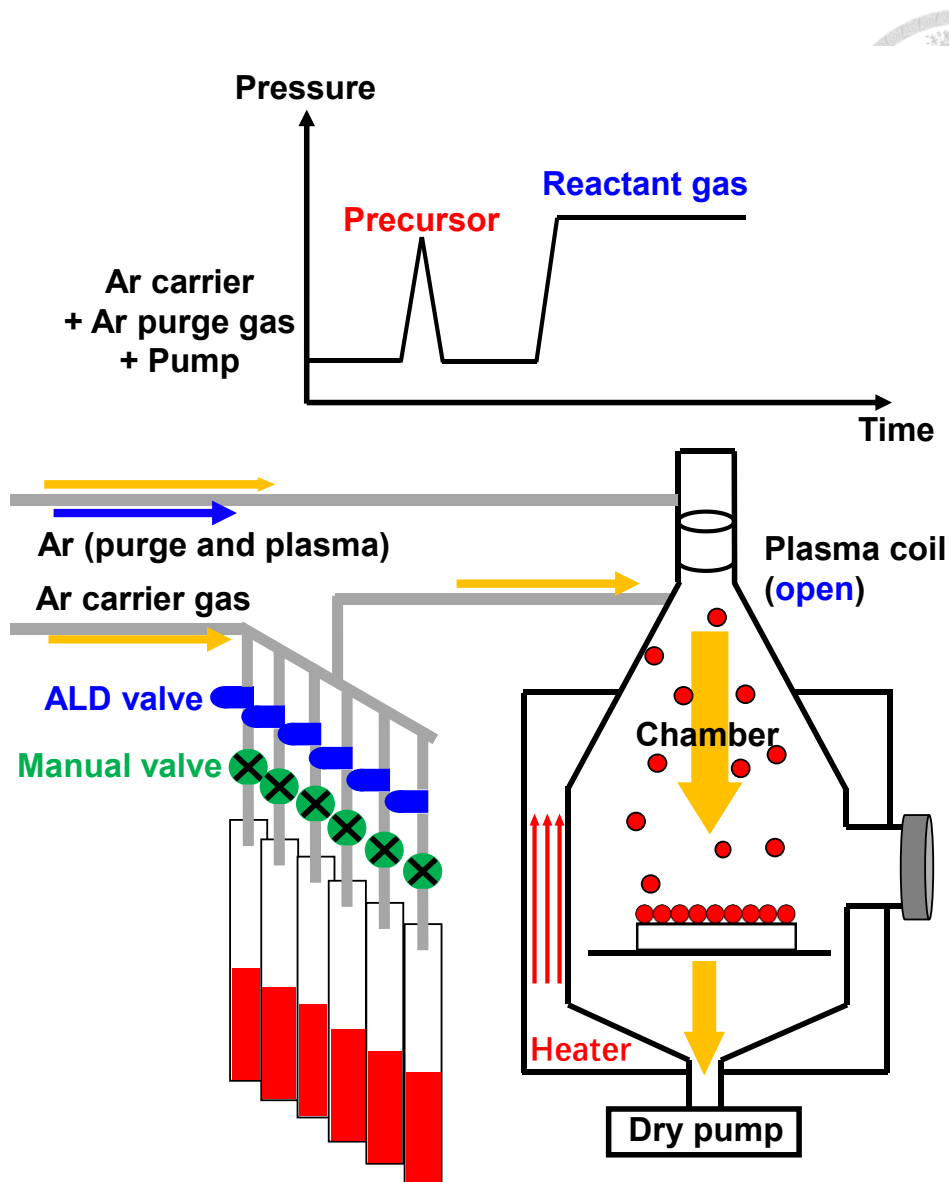
Fig. 2.2-2 Operation mode of single layer growth in PEALD.

2.3 MFM Capacitor Fabrication

To character the electrical properties, MFM capacitors were fabricated on Si substrates using the $Pt/TiN/Hf_{0.5}Zr_{0.5}O_2/TiN/Pt$ configuration (Fig. 2.3-1Fig. 2.3-1). The bottom Pt layer, deposited via sputtering, served as both an etch-stop layer and a probe layer[30, 31]. The PEALD process was carried out at a temperature of 250°C. The in-*situ* TiN bottom and top electrode deposition was achieved through PEALD using a forming gas mixture (50% N_2 + 50% H_2). Different exposure times of O_2 were performed to form alloys and superlattices[24]. The $Hf_{0.5}Zr_{0.5}O_2$ films consisted of 5 cycles of ZrO_2 followed by 5 cycles

9

of HfO_2, resulting in 50 cycles (Fig. 2.3-1). It is worth noting that using ZrO_2 as the first layer allowed for a higher $2P_r$ than using HfO_2 as the first layer[24]. Additionally, an in-*situ* forming gas plasma treatment was conducted on the TiN bottom electrodes to form distinct bottom-top interfaces. The precursor chemicals used were TDMAZr, TDMAHf, and TDMATi for ZrO_2, HfO_2, and TiN, respectively.
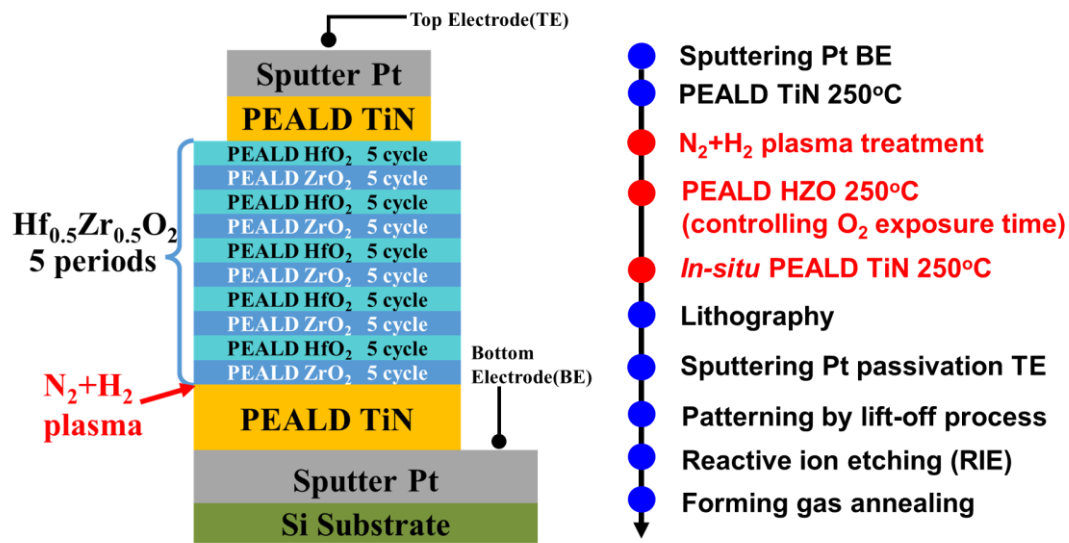
Fig. 2.3-1 Process flow of $Pt/TiN/Hf_{0.5}Zr_{0.5}O_2/TiN/Pt$ capacitor.

Following the PEALD process of $TiN/Hf_{0.5}Zr_{0.5}O_2/TiN/Pt$ (bottom), a top Pt passivation layer was sputtered and deposited to prevent oxidation on the TiN surface. This passivation layer was then patterned using the lift-off process. Subsequently, the $TiN/Hf_{0.5}Zr_{0.5}O_2/TiN$ films were etched until reaching the bottom Pt layer through reactive ion etching (RIE). After completing the device fabrication steps mentioned above, a PMA process was conducted in a forming gas mixture of 90% N_2 and 10% H_2. This annealing process aimed to crystallize the $Hf_{0.5}Zr_{0.5}O_2$ thin films. A PMA temperature of 450°C was applied for $Hf_{0.5}Zr_{0.5}O_2$ with a 5s O_2 exposure, while a temperature of 400°C was used for $Hf_{0.5}Zr_{0.5}O_2$ with a 10s O_2 exposure.

10

2.4 Material Analysis of Alloy and Superlattice $Hf_{0.5}Zr_{0.5}O_2$

TEM images illustrate the crystallinity and physical thickness of the FE layer. In accordance with the fabrication process, the bottom and top PEALD TiN electrodes are situated below and above the $Hf_{0.5}Zr_{0.5}O_2$ thin films, respectively. TEM images reveal a distinct metal-oxide interface, allowing for the estimation of the crystal thickness of $Hf_{0.5}Zr_{0.5}O_2$. The TEM image (Fig. 2.4-1(a)) demonstrates good crystallinity in the 6.3nm $Hf_{0.5}Zr_{0.5}O_2$ film with a 5s O_2 exposure time. Conversely, the 6.7nm $Hf_{0.5}Zr_{0.5}O_2$ film with a 10s O_2 exposure time shown in Fig. 2.4-1(b) exhibits higher crystallinity and is thicker compared to the film with a 5s O_2 exposure time due to the increased oxygen content in the PEALD process.

To seriously distinguish the alloy and superlattice structure, HAADF images are applied in this analysis. HAADF imaging is a technique used in scanning transmission electron microscopy (STEM) to provide atomic number contrast. It can distinguish elements based on their atomic number (Z)[32]. The contrast in HAADF imaging arises from the dependence of the scattering cross-section on the atomic number. Higher atomic number elements have a larger scattering cross-section due to their increased number of protons, resulting in stronger scattering and higher intensity in the HAADF image. Therefore, regions in the sample with elements of higher atomic numbers appear brighter in the image compared to areas with lower atomic numbers of elements. As a result, hafnium (Z=72) images brighter than Zirconium (Z=40) in HAADF.

The $Hf_{0.5}Zr_{0.5}O_2$ film with 5s O_2 exposure is an alloy with the ZrO_2-HfO_2 interfacial mixture, as shown in the HAADF image (Fig. 2.4-2(a)). In contrast, $Hf_{0.5}Zr_{0.5}O_2$ with 10s O_2 exposure shows clear ZrO_2-HfO_2 interfaces and superlattices (Fig. 2.4-2(b)). The dark layers (marked in dark blue) are ZrO_2 with PEALD 5 cycles in each layer, and the bright layers (marked in bright blue) are HfO_2 with PEALD 5 cycles in each layer.

11
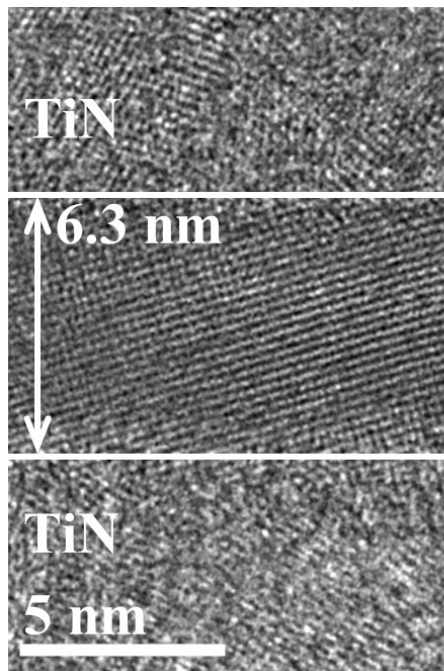
(a) O$_2$ exposure 5s **(b) O$_2$ exposure 10s**
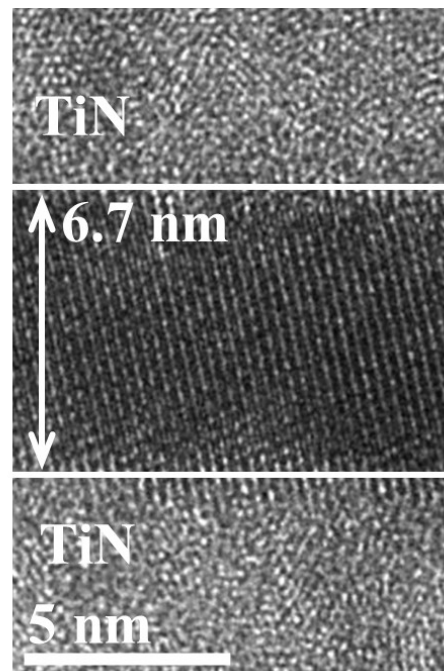
Fig. 2.4-1 TEM images with O$_2$ exposure time of (a) 5s and (b) 10s.
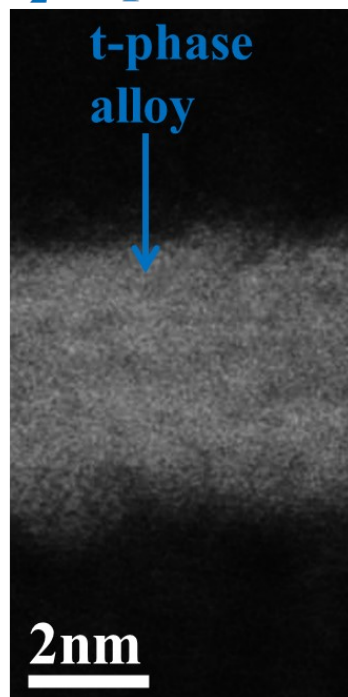
(a) O$_2$ exposure 5s **(b) O$_2$ exposure 10s**
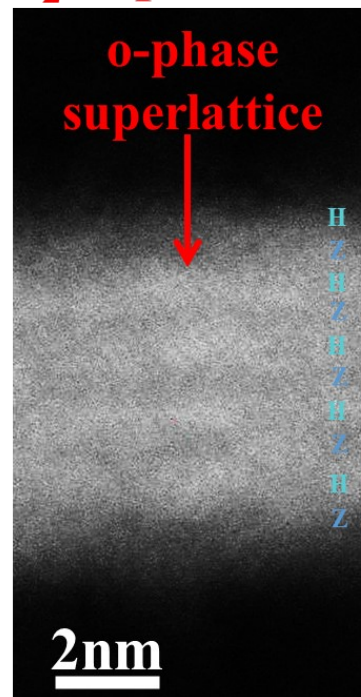
Fig. 2.4-2 HAADF images with O$_2$ exposure time of (a) 5s and (b) 10s.

12

2.5 Electrical Characteristics of Alloy and Superlattice $Hf_{0.5}Zr_{0.5}O_2$

Our previous research has extensively examined the effects of $[V_o]$[24]. In our MFM heterostructures, we utilize $[V_o]$ to manipulate the FE and AFE properties at room temperature. Higher $[V_o]$ results in the formation of alloys, promoting AFE behavior at room temperature. Conversely, lower $[V_o]$ leads to the formation of superlattices, favoring FE characteristics at room temperature. Furthermore, our findings suggest that $Hf_{0.5}Zr_{0.5}O_2$ with superlattice structures favors the formation of the o-phase, while $Hf_{0.5}Zr_{0.5}O_2$ alloys facilitate the creation of the t-phase with a relatively high dielectric constant.

The $Hf_{0.5}Zr_{0.5}O_2$ with 5s O_2 exposure exhibited an AFE polarization-voltage (P-V) loop at 300K, as shown in Fig. 2.5-1. This observation suggests that the high $[V_o]$ and alloys favored the formation of the t-phase. At 300K, the t-phase characteristics were consistently observed with four peaks in both the forward and reverse capacitance-voltage (C-V) sweeps, as shown in Fig. 2.5-2.

Due to o-phase favoring low $[V_o]$ and superlattices, the pristine P-V loop at 300K shows FE characteristics with $2Pr = 44\mu C/cm^2$ in Fig. 2.5-3. Meanwhile, the coercive voltage $(2V_c)$ at 300K is 1.6V. Besides, the C-V hysteresis shows two peaks in the forward and reverse C-V sweeps (Fig. 2.5-4), indicating FE o-phase dominance.

13
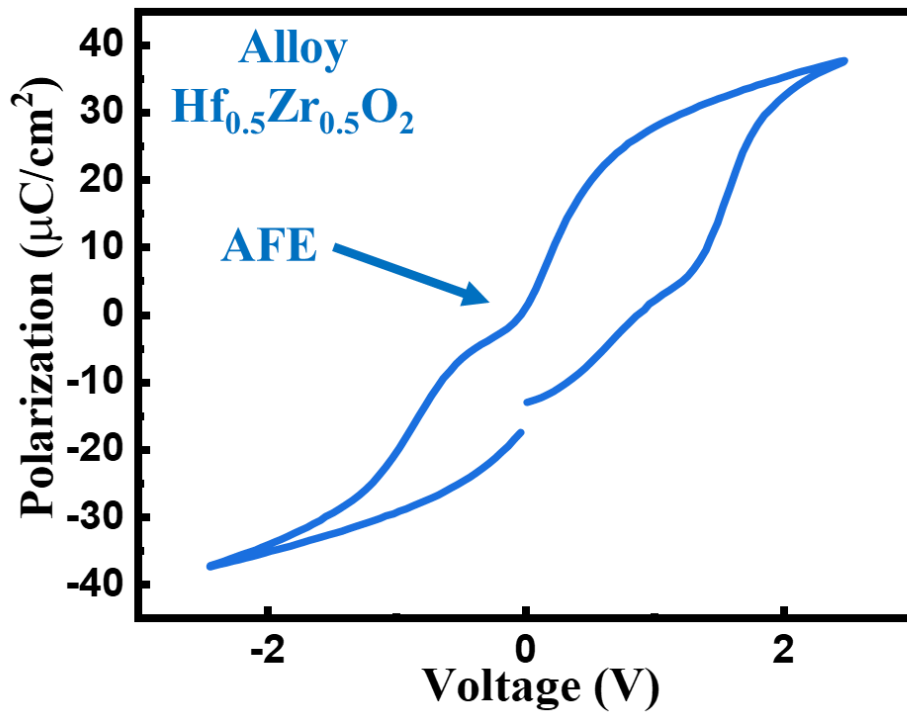
Fig. 2.5-1 P-V loop of $Hf_{0.5}Zr_{0.5}O_2$ alloys with O_2 exposure 5s measured at 300K.
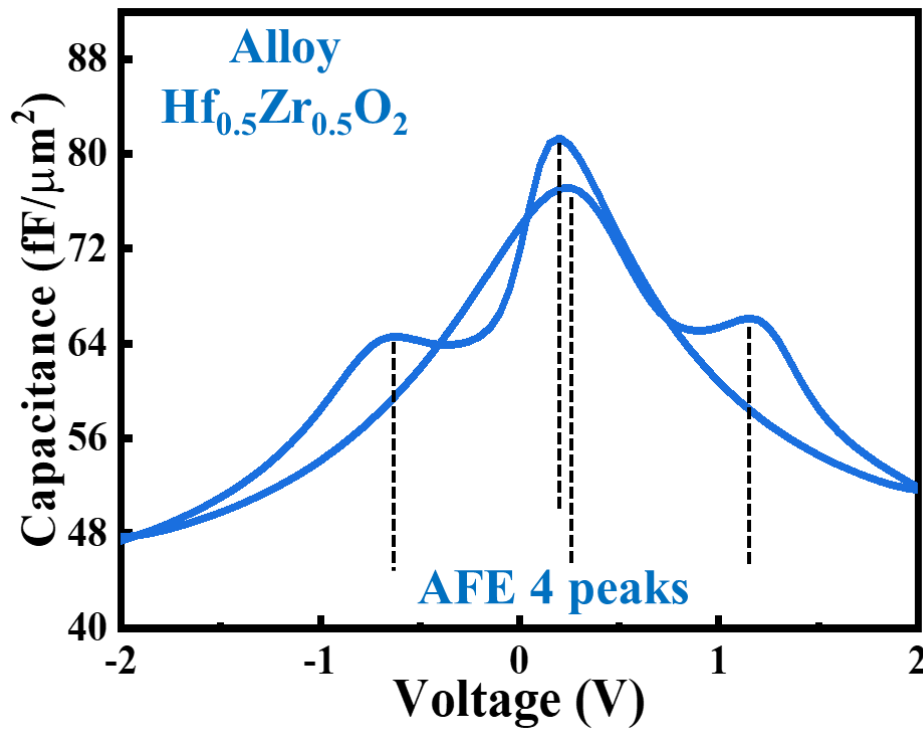
Fig. 2.5-2 C-V curve of $Hf_{0.5}Zr_{0.5}O_2$ alloys with O_2 exposure 5s measured at 300K.

14
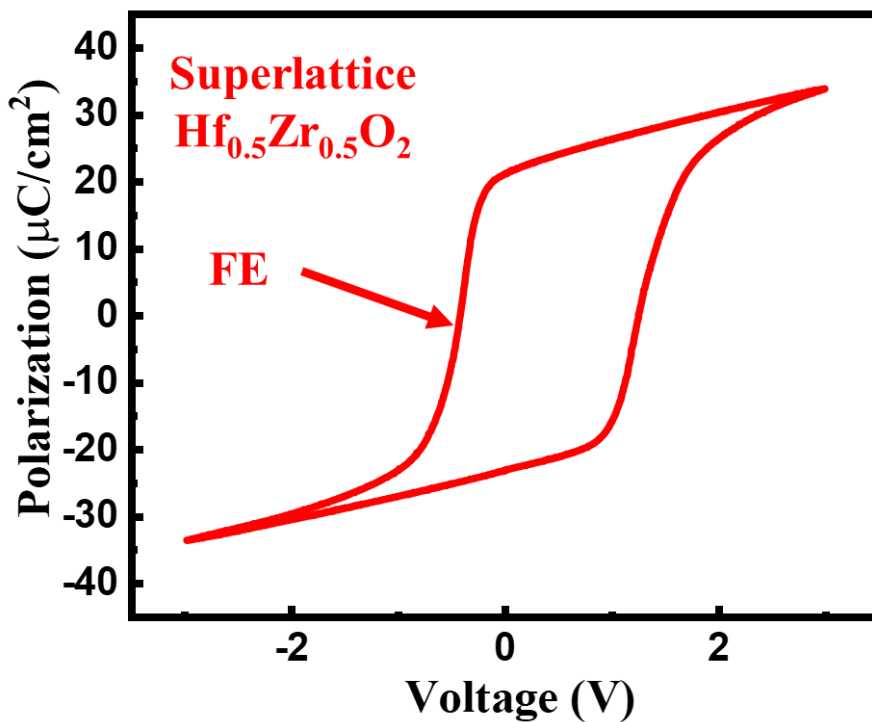
Fig. 2.5-3 P-V loop of $Hf_{0.5}Zr_{0.5}O_2$ superlattices with O_2 exposure 10s measured at 300K.
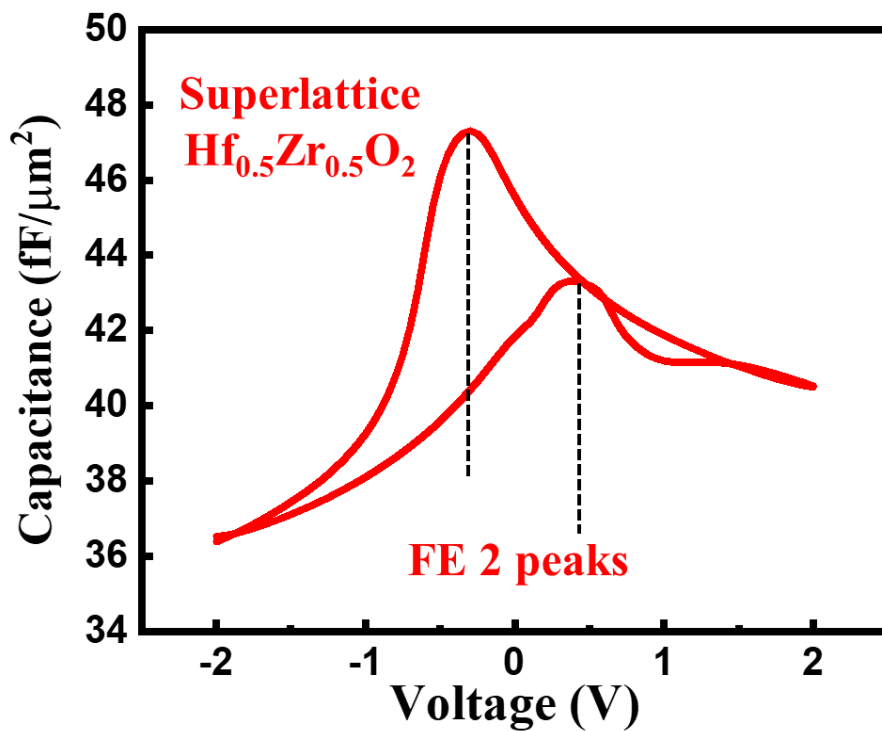
Fig. 2.5-4 C-V curve of $Hf_{0.5}Zr_{0.5}O_2$ superlattices with O_2 exposure 10s measured at 300K.

15

2.6 Dielectric Constant of $Hf_{0.5}Zr_{0.5}O_2$ with Different O_2 Exposure Time

The dielectric constant of $Hf_xZr_{1-x}O_2$ is primarily influenced by the presence of different crystalline phases, including the monoclinic phase, FE o-phase, and AFE t-phase. Generally, a lower $[V_o]$ in the material favors the formation of the FE o-phase, while a higher $[V_o]$ promotes the AFE t-phase. These distinct crystalline phases contribute to the overall dielectric constant of $Hf_xZr_{1-x}O_2$.

Table 2-1 illustrates the κ value of m-phase, o-phase, and t-phase in HfO_2 and ZrO_2 [23, 33, 34]. Note that the t-phase has the highest theoretical κ value among all three phases, which is 70 of HfO_2 and 47 of ZrO_2. Non-hysteretic C-V measurement at 100 kHz is used to extract the κ value of $Hf_{0.5}Zr_{0.5}O_2$.

Fig. 2.6-1 shows non-hysteretic C-V curves of $Hf_{0.5}Zr_{0.5}O_2$ measured at low voltage sweep C-V. The κ value is 30, 36, 42, and 47 for O_2 exposure 15s, 10s, 5s, and 3s, respectively. With O_2 exposure time decreasing and more $[V_o]$ existing, high-κ t-phase become more favoring, resulting in the increase of κ value.

Table 2-1 Dielectric constant of m-, o-, and t-phase.

Dielectric constant	Monoclinic	Orthorhombic	Tetragonal
HfO_2	16 [33]	27 [23]	70 [33]
ZrO_2	20 [34]	31 [23]	47 [34]

16
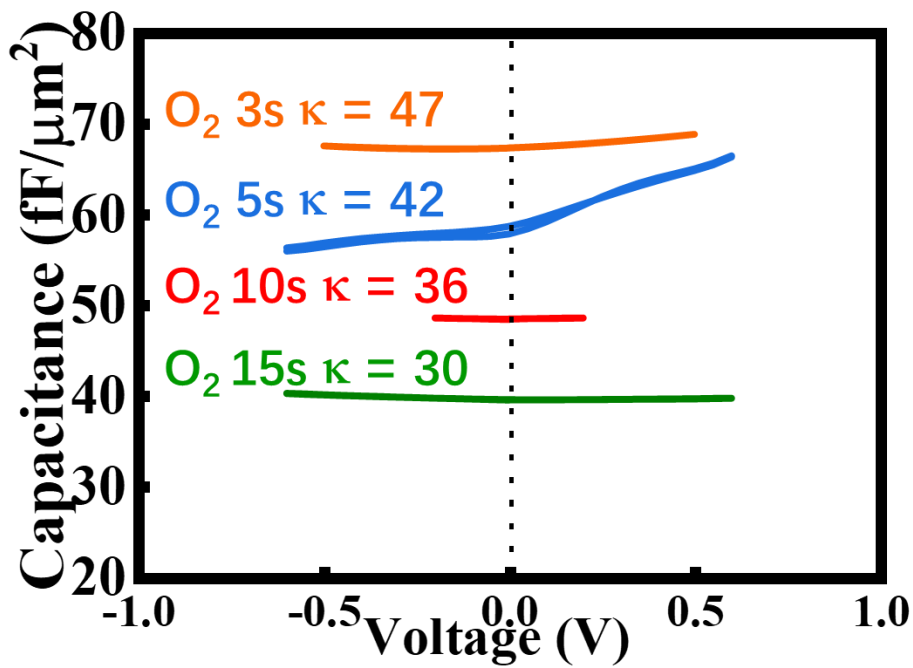
Fig. 2.6-1 Dielectric constant of $Hf_{0.5}Zr_{0.5}O_2$ with various O_2 exposure times.

2.7 Summary

The PEALD MFM capacitors with different O_2 exposure times are fabricated to investigate the $[V_o]$ effect on $Hf_{0.5}Zr_{0.5}O_2$. Low $[V_o]$ and superlattice structure are concluded in FE o-phase favoring. In contrast, high $[V_o]$ and alloy structure are concluded in AFE t-phase favoring by material and electrical characteristics analysis, respectively. Besides, the dielectric constant of $Hf_{0.5}Zr_{0.5}O_2$ with different $[V_o]$ is extracted by non-hysteretic C-V measurement to prove that increasing $[V_o]$ helps high-κ t-phase formation and contributes to the increase of κ value.

17

Chapter 3 - Cryogenic Phase Transition

3.1 Introduction

The identification of the o-phase and t-phase in $Hf_{0.5}Zr_{0.5}O_2$ films can be challenging due to the overlapping peak positions in grazing incident X-ray diffraction (GIXRD) spectra. However, observing variations in the P_r values can confirm the phase transition. Additionally, in [35], density functional theory (DFT) models for interfacial energy calculations have been reported.

This chapter proposes a cryogenic phase transition model to investigate the transition from t-phase to o-phase during cooling temperatures. Experimental measurements validate this model. The cryogenic phase transition occurs below the Curie temperature (T_{curie}) and can be fitted using the LDG theory. The phase transition kinetics are described using predicted free energies of the m-phase, o-phase, and t-phase obtained from the DFT study, as well as the barrier energies of the phase transition.

3.2 Cryogenic Measurement of Alloy $Hf_{0.5}Zr_{0.5}O_2$

The $Hf_{0.5}Zr_{0.5}O_2$ thin film with a 5s O_2 exposure exhibited an AFE P-V loop at 300K, indicating a high $[V_o]$ and an alloy structure that favored the t-phase. As the temperature is lowered, the free energy of the t-, m-, and o-phases becomes temperature-dependent, leading to transformations in the electrical characteristics[36, 37].

At 220K, the P-V loop exhibits FE properties, as shown in Fig. 3.2-1. Further cooling to 150K and 77K maintains the stability of the FE P-V loops, accompanied by an increase in the 2Pr values. Upon heating back up to 300K, the P-V loop reverses from FE to AFE (Fig. 3.2-2).

18

To confirm the transition from AFE to FE during cooling, C-V sweeps are measured at various temperatures: 300K, 220K, 150K, 77K, and 300K (heating up after cooling), as depicted in Fig. 3.2-3 and Fig. 3.2-4. At 300K, consistent with previous observations, the t-phase characteristics are evident, with four peaks in both the forward and reverse C-V sweeps. A transition from AFE (four peaks) to FE (two peaks) in the C-V hysteresis is observed during cooling, consistent with the findings from the P-V loops. Upon returning to room temperature, the 5s exposure sample exhibits an AFE P-V loop with four peaks in the C-V hysteresis. These reversible transitions from AFE to FE and back to AFE confirm the feasibility of overcoming the energy barrier between the o-phase and t-phase reversibly.
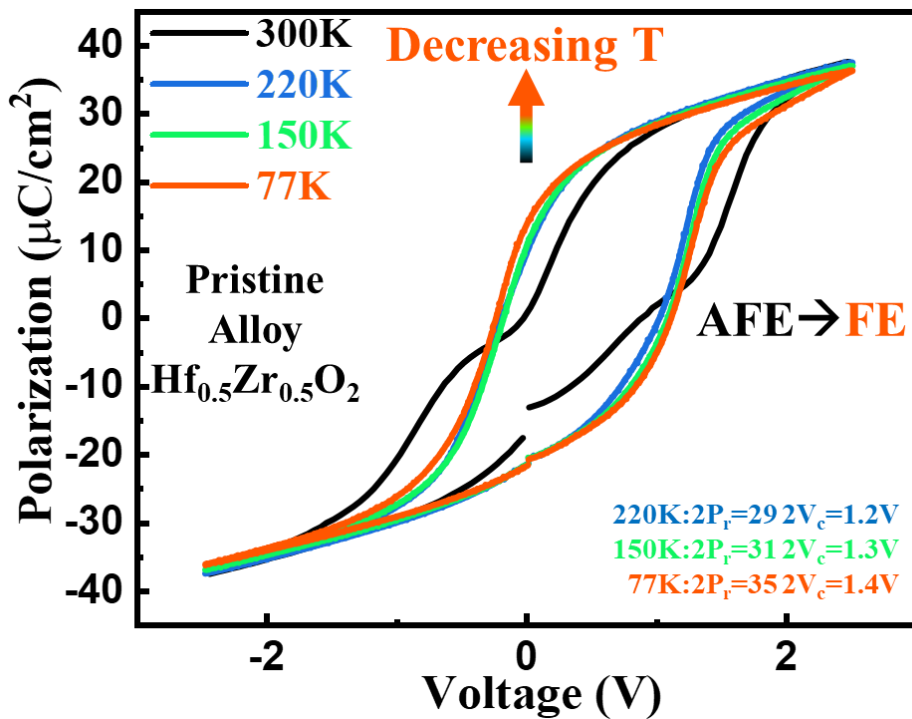
Fig. 3.2-1 P-V loops of $Hf_{0.5}Zr_{0.5}O_2$ alloys with O_2 exposure 5s measured at 300K, 220K, 150K, and 77K.

19
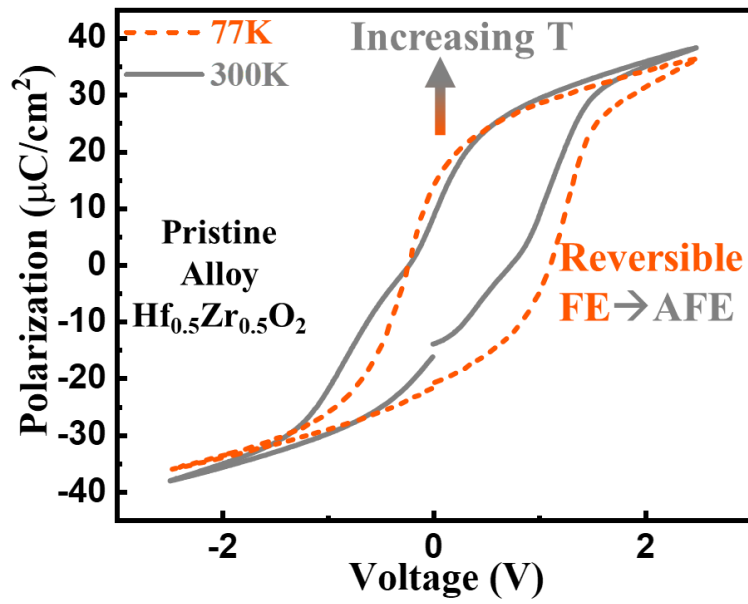
Fig. 3.2-2 P-V loops of $Hf_{0.5}Zr_{0.5}O_2$ alloys with O_2 exposure 5s measured by heating up to 300K.
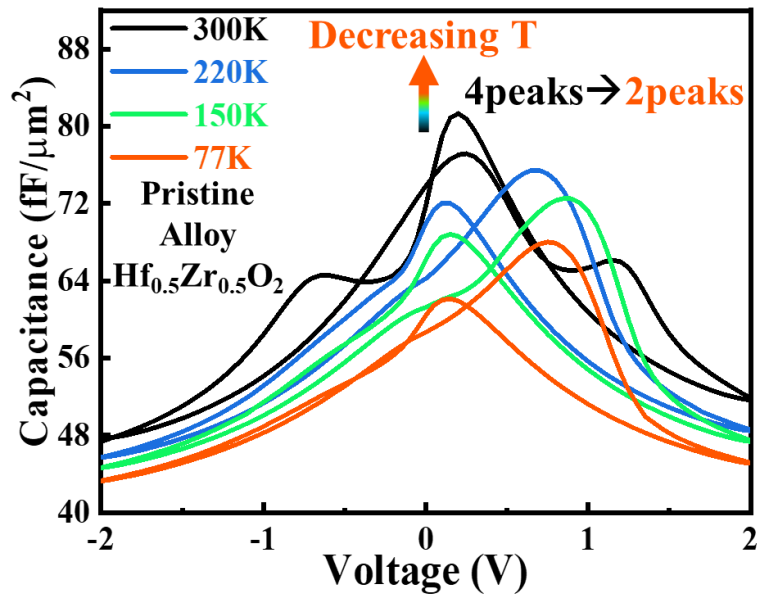
Fig. 3.2-3 C-V curves of $Hf_{0.5}Zr_{0.5}O_2$ alloys with O_2 exposure 5s measured at 300K, 220K, 150K, and 77K.
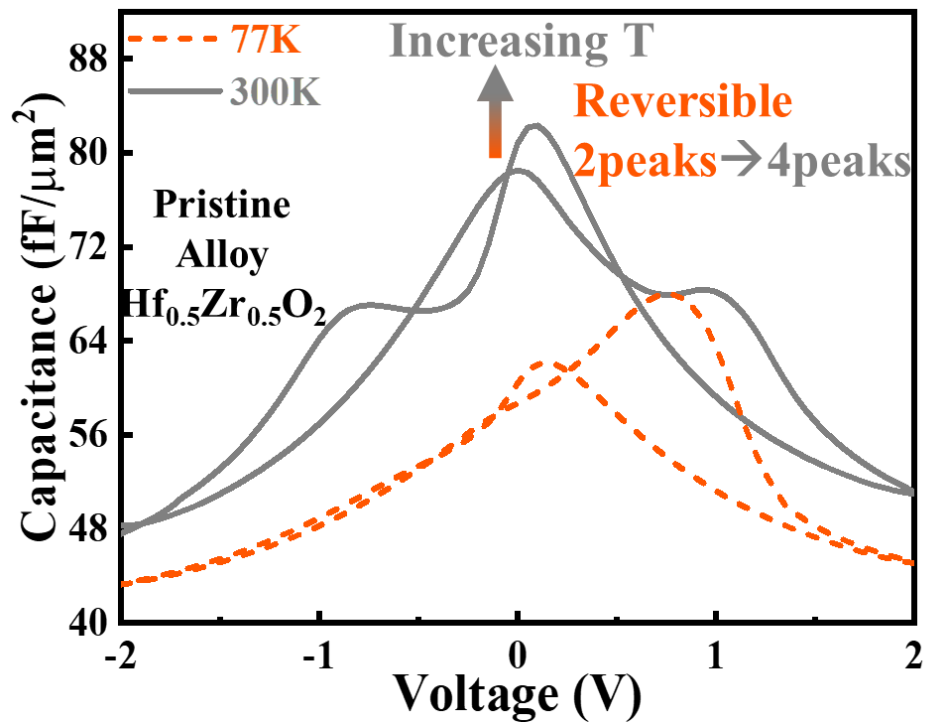
Fig. 3.2-4 C-V curves of $Hf_{0.5}Zr_{0.5}O_2$ alloys with O_2 exposure 5s measured by heating up to 300K.

3.3 Cryogenic Measurement of Superlattice $Hf_{0.5}Zr_{0.5}O_2$

To further investigate the t- to o-phase transition and its impact on FE enhancement at cryogenic temperatures, we fabricated an $Hf_{0.5}Zr_{0.5}O_2$ thin film with a 10s O_2 exposure. The longer exposure time promotes the formation of the o-phase due to its preference for low [V_o] and superlattice structures. As a result, the pristine P-V loop at 300K exhibits FE characteristics.

At 77K, the $Hf_{0.5}Zr_{0.5}O_2$ thin film demonstrates a stable FE P-V loop with an improved $2P_r$ value of 54 $\mu C/cm^2$, indicating an enhanced amount of the o-phase resulting from the transition from the t-phase (Fig. 3.3-1). This represents a 23% improvement compared to the previous observation at room temperature. Additionally, the coercive voltage (V_c) increases as the temperature decreases, indicating a stronger resistance to polarization switching[38].

21

The C-V hysteresis exhibits consistent behavior with two peaks, suggesting the dominance of the FE phase during the cooling process. This aligns with the observed transition from AFE to FE properties in Fig. 3.2-1 and Fig. 3.2-3. Therefore, the cooling process serves to diminish the t-phase and enhance the o-phase, leading to improved ferroelectricity.
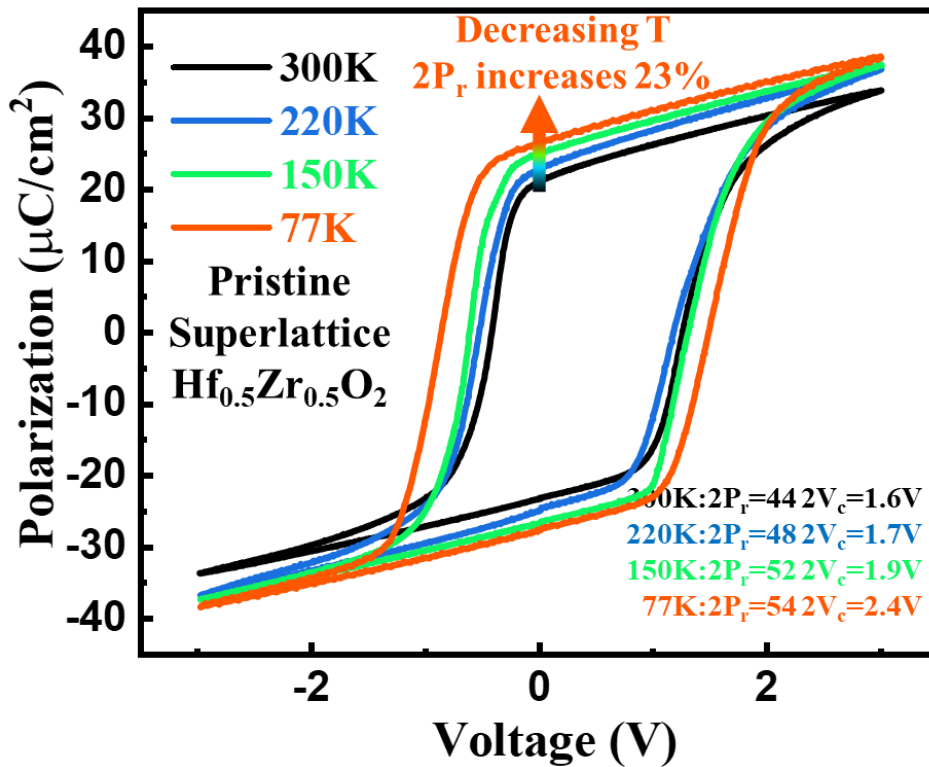
Fig. 3.3-1 P-V loops of $Hf_{0.5}Zr_{0.5}O_2$ superlattices with O_2 exposure 10s measured at 300K, 220K, 150K, and 77K.
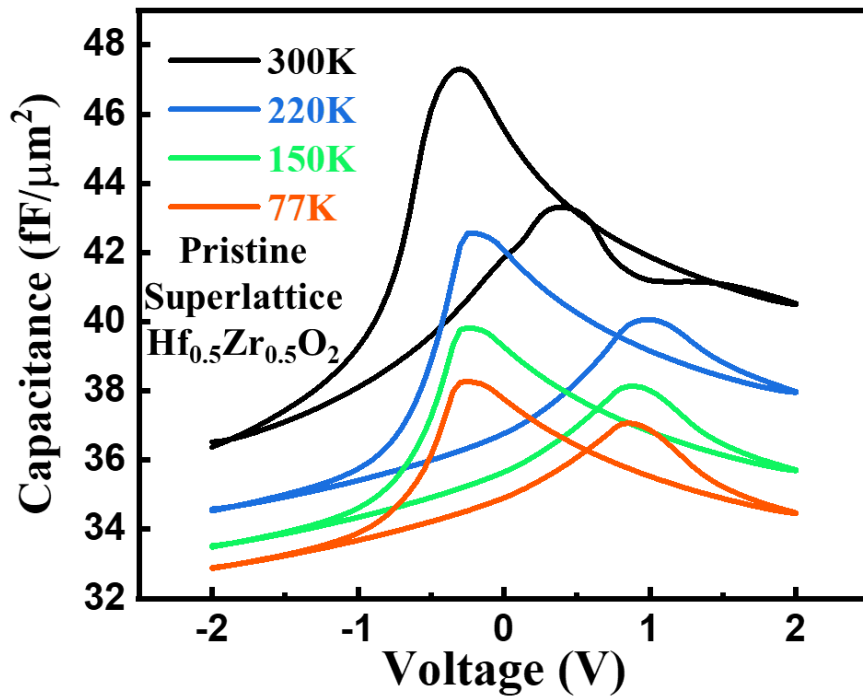
Fig. 3.3-2 C-V curves of $Hf_{0.5}Zr_{0.5}O_2$ superlattices with O_2 exposure 10s measured at 300K, 220K, 150K, and 77K.

3.4 Landau-Ginzburg-Devonshire (LGD) Theory

In the context of LGD theory, the temperature-dependent phase transition is explained using the concept of intrinsic switching[39]. The thermodynamic free energy (G) is expressed as a polynomial expansion of the polarization (P) up to the sixth order:

$$G(T) = \frac{\alpha(T)}{2}P^2 + \frac{\beta}{4}P^4 + \frac{\gamma}{6}P^6 - PE. \qquad (3.4.1)$$

In this expansion, the coefficients α, β, and γ are temperature-independent Landau coefficients, and E represents the electric field. The reciprocal of the dielectric susceptibility is denoted by α, which is linearly related to temperature.

The reversible phase transition between the o-phase and t-phase occurs below the T_{curie}. Based on this premise, the energy polynomial expansion can be simplified and truncated to the fourth order. The sign of α remains negative below T_{curie}, and its

23

magnitude decreases with decreasing temperature. The electric field across the FE material at thermal equilibrium can be determined by differentiating the free energy concerning polarization ($\partial G / \partial P = 0$), as given by Eq. (3.4.1).

$$E = \alpha P + \beta P^3 \qquad (3.4.2)$$

The LGD theory provides a simplified description of polarization hysteresis using Eq. (3.4.2), which involves two crucial coefficients associated with phase transitions. For the convenient calculation, γ is not been considered due to its small order of magnitude. The intrinsic switching model can be formulated using the coefficients α and β by utilizing experimental data on P_r and V_c. The remanent polarization value can be determined by setting the electric field (E) to zero, yielding the relationship stated in Eq. (3.4.3).

$$P = \sqrt{\frac{-\alpha}{\beta}} \qquad (3.4.3)$$

And, according to the free energy description, following with the Curie-Weiss behavior, the coefficient α:

$$\alpha = \alpha_0(T - T_{curie}), \qquad (3.4.4)$$

Where α_0 is a positive constant. To determinate the coercive field (E_C), the electric field at local extremes need to be analyzed,

$$E_C = \pm\frac{2}{3}\alpha_0(T - T_{curie})\sqrt{\frac{-\alpha_0(T - T_{curie})}{3\beta}} \qquad (3.4.5)$$

By utilizing Equations (3.4.3) and (3.4.5), the coefficients α_0 and β can be extracted from the experimental data of $Hf_{0.5}Zr_{0.5}O_2$. In the analysis of $Hf_{0.5}Zr_{0.5}O_2$ with 5s O_2 exposure, the gradual transition from AFE to FE spanned between 300K and 220K. As a result, the AFE data are excluded from the analysis[40].

During the cooling process, there is a steady increase in P_r value, leading to an

24

enhancement of ferroelectricity as the t-phase transitions to the o-phase (as shown in Fig. 3.4-1). It should be noted that the T_{curie} of $Hf_{0.5}Zr_{0.5}O_2$ with 5s O_2 exposure is determined to be 622K through the best fit of the LGD model using our experimental data. Furthermore, the progressively enhanced ferroelectricity causes the average V_c to increase during the cooling process (as illustrated in Fig. 3.4-2).

Fig. 3.4-1 Fitting results using the LGD model from $Hf_{0.5}Zr_{0.5}O_2$ alloys with O_2 exposure 5s of remanent polarization vs. temperatures.

25

$$V_c = |\frac{2}{3} * \alpha_0 (T - T_{curie}) * \sqrt{\frac{-\alpha_0 (T - T_{curie})}{3\beta}} * t_{FE}|$$
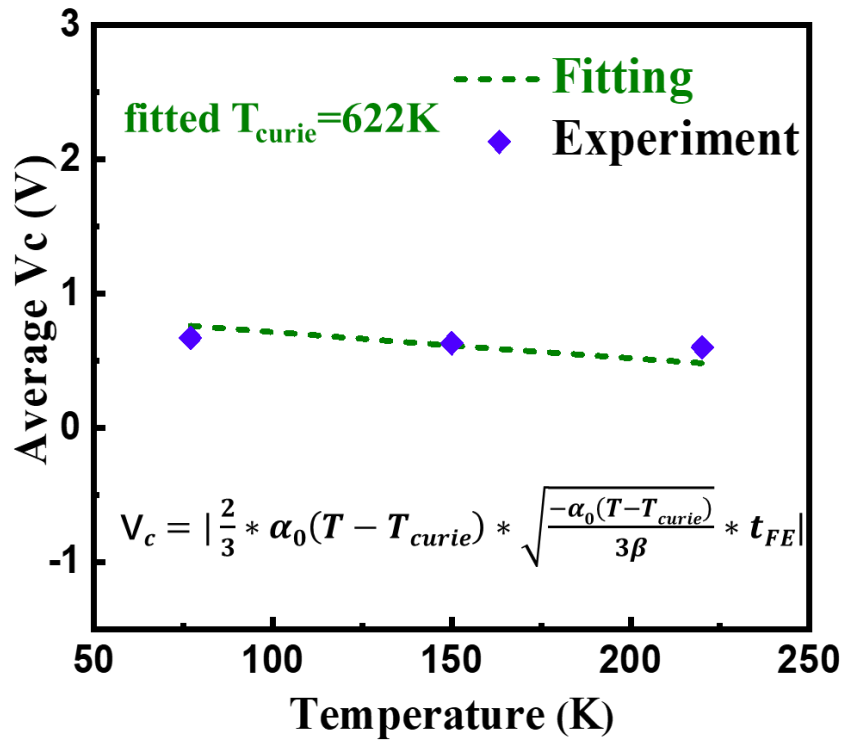
Fig. 3.4-2 Fitting results using the LGD model from $Hf_{0.5}Zr_{0.5}O_2$ alloys with O_2 exposure 5s of average V_c vs. temperatures.

In order to further investigate the enhancement of ferroelectricity through the t- to o-phase transition, $Hf_{0.5}Zr_{0.5}O_2$ with 10s O_2 exposure was studied. The T_{curie} is determined to be 732K through the best fit of the LGD model using the experimental data shown in Fig. 3.4-3 and Fig. 3.4-4. This value aligns with the reported T_{curie} for similar $Hf_xZr_{1-x}O_2$ systems[37, 41-43].

$$\varepsilon_r = \frac{\partial E}{\partial P} = \frac{1}{\alpha_0 (T_{curie} - T) + 3\beta P^2} \qquad (3.4.6)$$

Comparing the estimated α_0 (1.7E6 $VmK^{-1}C^{-1}$) from the temperature-dependent permittivity (ε_r) in the Curie-Weiss law (Eq. (3.4.6)), the fitted α_0 (2.7E6 $VmK^{-1}C^{-1}$) from our data using the LGD theory is reasonably close. It should be noted that the dielectric constant measurements are performed at low voltage without hysteresis due to the presence of hysteresis in the C-V measurement.

26

The $Hf_{0.5}Zr_{0.5}O_2$ film with 10s O_2 exposure contains fewer $[V_o]$ than the film with 5s O_2 exposure, which increases T_{curie} [37]. Additionally, the Pr value shows a 23% improvement from 300K to 77K (Fig. 3.4-3). The transition from the t-phase to the o-phase at lower temperatures occurs with a low energy barrier, leading to a greater amount of o-phase. Moreover, the average V_c follows a linear trend, indicating increased FE enhancement[44, 45]. Cryogenic temperatures effectively compensate for the loss of memory window (MW $\approx 2V_c$) caused by the thin film.

The T_{curie} plays a crucial role in forming the FE o-phase during the cooling process. To promote the formation of more o-phase, the amount of $[V_o]$ can be reduced during the fabrication process, increasing the T_{curie}. While the LGD theory can explain the cryogenic phase transition in the material's properties, it does not incorporate the intrinsic phase transition mechanism due to the absence of energy barriers. Therefore, the kinetic energy barriers between each phase are critical for understanding the physical mechanism of cryogenic behavior based on the experimental data.
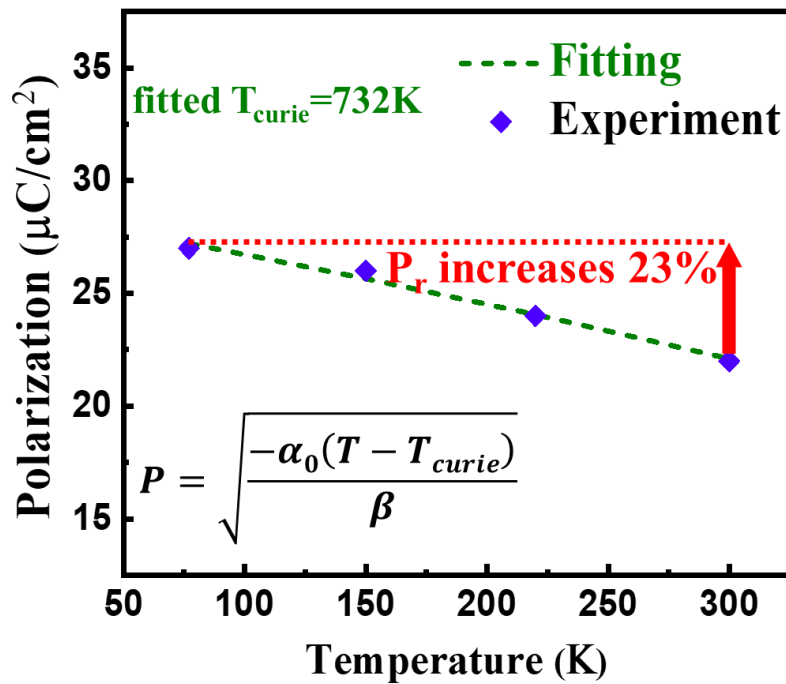
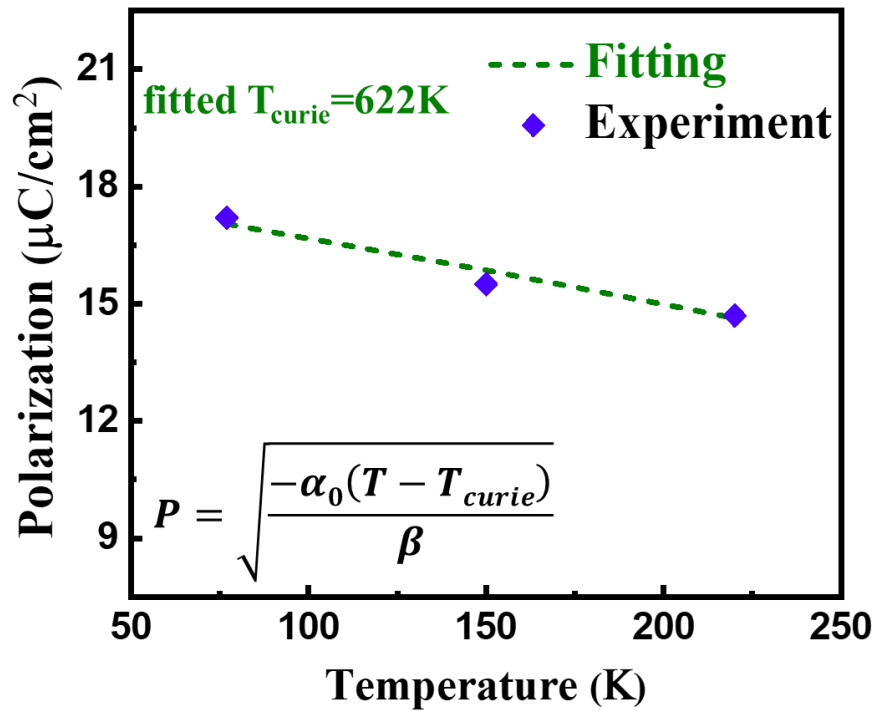Fig. 3.4-3 Fitting results using the LGD model from $Hf_{0.5}Zr_{0.5}O_2$ superlattices
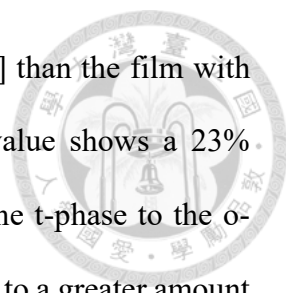with O_2 exposure 10s of remanent polarization vs. temperatures.
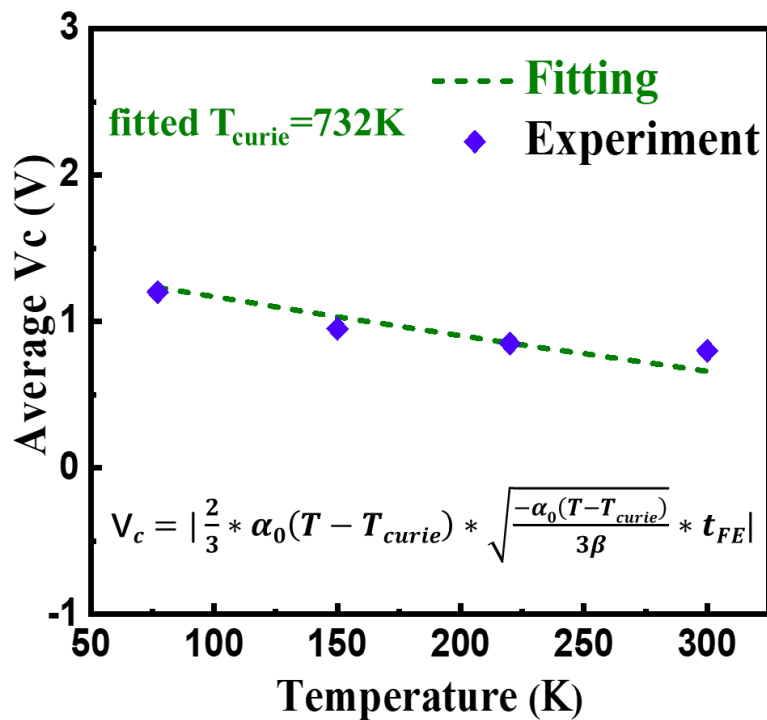
Fig. 3.4-4 Fitting results using the LGD model from $Hf_{0.5}Zr_{0.5}O_2$ superlattices
with O_2 exposure 10s of average V_c vs. temperatures.

28
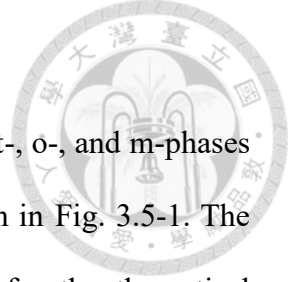
3.5 First-principle Calculation

To gain a better understanding, the relative free energies of the t-, o-, and m-phases in $Hf_{0.5}Zr_{0.5}O_2$, dependent on temperature, were calculated as shown in Fig. 3.5-1. The $Hf_{0.5}Zr_{0.5}O_2$ film with 5s O_2 exposure was used as a reference for the theoretical calculations, consistent with the LGD analyses. The phase free energy (Eq. (3.5.1)) comprises bulk energy, entropy contribution, and interfacial energy (Eq. (3.5.2))[46, 47].
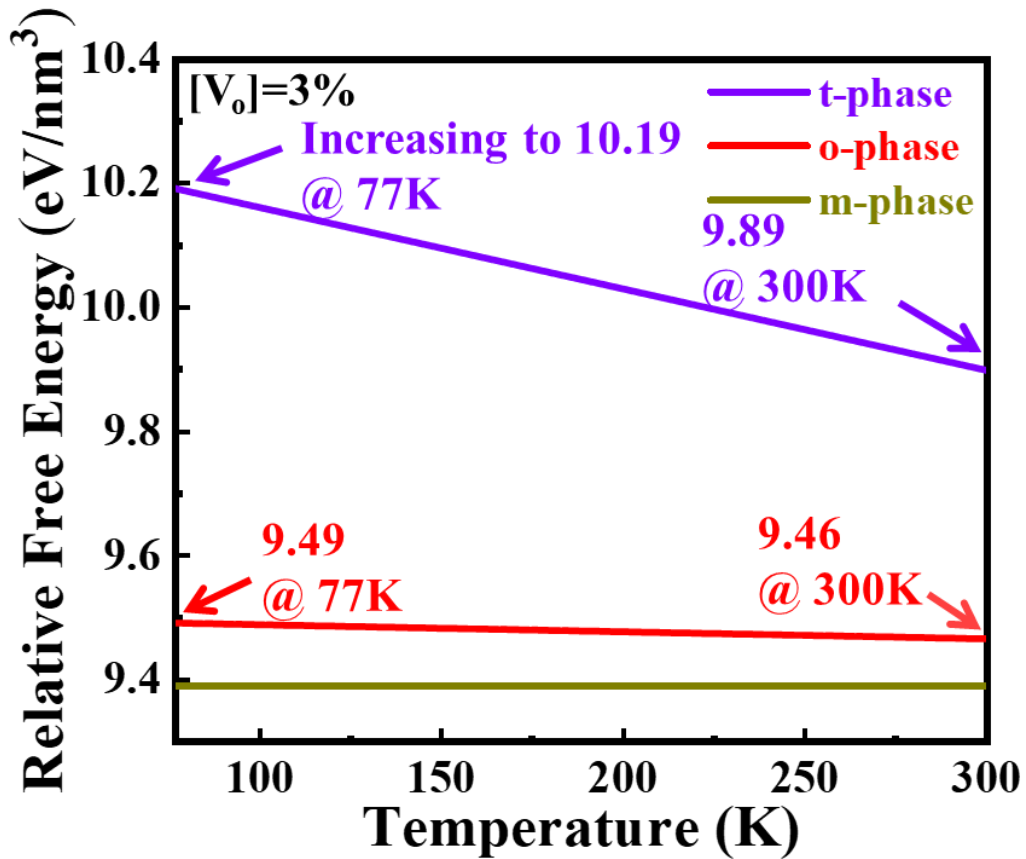
Fig. 3.5-1 Relative free energy of o-, t-, and m-phase with $[V_o]$=3% under various temperatures.

$$G_i = U_i - TS_i + \Gamma_i \qquad (3.5.1)$$

$$\Gamma_i = \frac{2\pi(r^2 \times \sigma_i + rd \times \delta_i)}{\pi r^2 d} \qquad (3.5.2)$$

The index "i" represents the phase in the $Hf_{0.5}Zr_{0.5}O_2$ film, which could be the m-

29

phase, o-phase, or t-phase. G_i, U_i, S_i, and Γ_i denote the phase free energy, relative bulk energy, entropy, and interfacial energy, respectively. For computational convenience, the relative bulk energy of the m-phase is assumed to be zero.

According to the assumption of cylindrical grain growth in the $Hf_{0.5}Zr_{0.5}O_2$ film, the interfacial energy Γ_i is a function of the interfacial energy of $Hf_{0.5}Zr_{0.5}O_2$/ILs (σ_i) (Table 3-1), the estimated radius of the grain size (r≈6nm) based on experimental data for $Hf_{0.5}Zr_{0.5}O_2$ [48], the thickness of $Hf_{0.5}Zr_{0.5}O_2$ (d=6.3nm), and the crystalline phase/amorphous $Hf_{0.5}Zr_{0.5}O_2$ interfacial energy (δ_i) (Table 3-1), as shown in Eq. (3.5.2). It should be noted that the assumed grain size radius (r≈6nm) is based on the experimental thickness. G_i, U_i, S_i, and Γ_i values were calculated using density functional theory (DFT). In our calculation, the value of Γ_i was found to be 9.58 eV/nm^3 for the m-phase, 8.45 eV/nm^3 for the o-phase, and 7.54 eV/nm^3 for the t-phase. The t-phase stability decreases with decreasing temperature as its free energy increases.

Table 3-1 Interfacial energies of HZO/ILs [46]

Interfacial Energies of HZO/ILs (J/m^2)	α-HfO$_2$ (δ_i)	TiN (σ_i)
m-phase	1.17	3.25
o-phase	1.52	3.03
t-phase	0.82	3.00

Based on the DFT calculations, the calculated relative free energy can be translated into a free energy landscape (Fig. 3.5-2), along with the reported energy barriers for phase transitions (Table 3-2). It is important to note that the explanations provided by the LGD theory exclusively describe second-order phase transitions phenomenologically. The

30

relative free energy (G_i) (Eq. (3.5.1), dependent on bulk energy (U_i), temperature (T), entropy (S_i), and interfacial energy (Γ_i)) for the t-phase continues to increase. At the same time, that of the other two phases remains relatively stable during cooling (Fig. 3.5-1). The activation barriers reported in the literature are listed in Table 3-2.

Due to the much higher energy barrier between the t- and m-phases compared to the t- and o-phases (Table 3-2), the t-phase prefers to transition to the o-phase rather than the m-phase (Fig. 7(b))[20, 49-52]. Considering the capping effect in our samples, the activation barrier between the t- and m-phases has a higher value of 1.2 eV f.u.$^{-1}$ to 2.14 eV f.u.$^{-1}$, suppressing the formation of the m-phase during the cooling step, similar to previous studies[53].

As the temperature decreases from 300K to 77K, the relative free energy of the t-phase increases from 9.89 eV/nm^3 to 10.19 eV/nm^3, while the energy barrier between the t- and o-phases decreases (Fig. 3.5-2). Consequently, more o-phase is observed at 77K, which aligns with the observed boost in $2P_r$ in the experiments. Additionally, the lower energy barrier between the t- and o-phases (20~35 meV f.u.$^{-1}$, [20, 54-57]in Table 3-2) provides a favorable path for the cryogenic phase transition from the t- to o-phase.

The reversible transition between the AFE and FE confirms that the activation barrier between the t- and o-phases is compatible with KT (26 meV@300K). This indicates that most equilibrium can be reached at the experimental temperature.
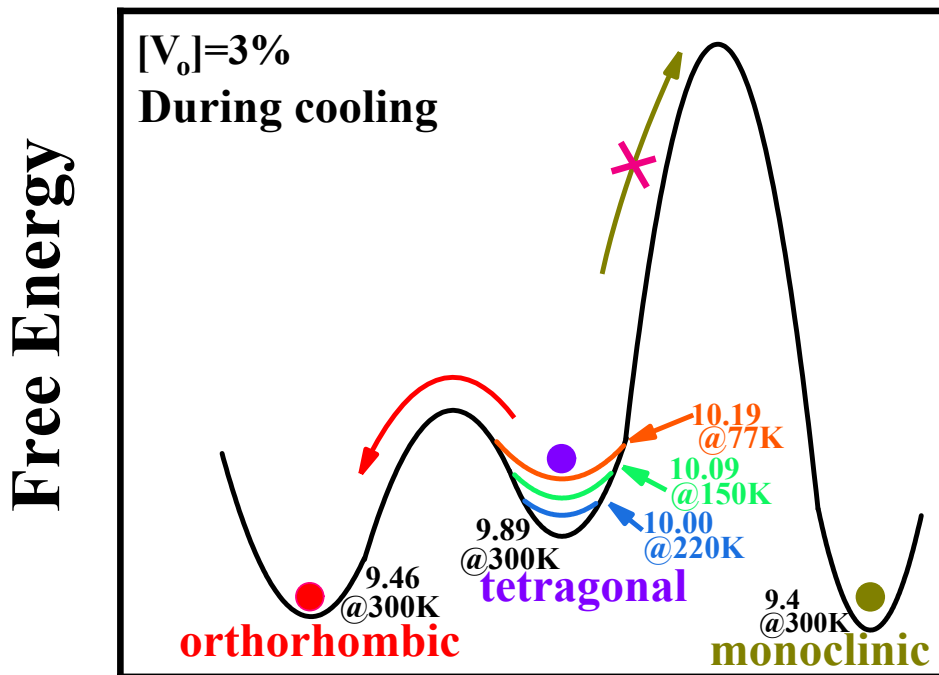
Fig. 3.5-2 Schematic diagram of free energy for the phase transition during cooling process. The relative barrier height between o- and t-phase decreases with decreasing temperature, indicating the transition from t-phase to o-phase is more favorable.

Table 3-2 Activation barriers between t/m phase and t/o-phase

t/m-phase	w/o capping	45 meV f.u.$^{-1}$ [49]	315 meV f.u.$^{-1}$ [20]	208 meV f.u.$^{-1}$ [50]
	capping	1.2 eV f.u.$^{-1}$ [51]	2.14 eV f.u.$^{-1}$ [52]	
t/o-phase	w/o capping	30 meV f.u.$^{-1}$ [20]	20 meV f.u.$^{-1}$ [54]	27 meV f.u.$^{-1}$ [55]
	capping	35 meV f.u.$^{-1}$ [56]	23.4 meV f.u.$^{-1}$ [57]	

32

3.6 Summary

Indeed, the experimental and theoretical findings support the clear cryogenic phase transition in $Hf_{0.5}Zr_{0.5}O_2$ film and provide an explanation for the observed enhancement of FE properties. The 23% improvement in $2P_r$, with a high value of 54 $\mu C/cm^2$ at 77K, demonstrates the effectiveness of the cryogenic phase transition.

The increase in the relative free energy of the t-phase plays a crucial role in reducing the energy barrier for the transformation to the o-phase. This decrease in the energy barrier facilitates the higher content of the o-phase in the $Hf_{0.5}Zr_{0.5}O_2$ film, leading to the observed boost in ferroelectricity.

Overall, the combination of experimental results and theoretical understanding confirms the significance of cryogenic phase transition in $Hf_{0.5}Zr_{0.5}O_2$ films and its impact on improving the FE properties, as indicated by the increased $2P_r$ values.

Chapter 4 - Thickness Effect in Ferroelectric Film
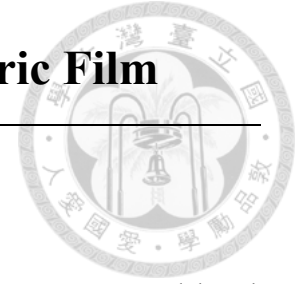
4.1 Introduction

FTJs, serving as FE NVMs, exhibit unique attributes such as nanosecond-level write/erase speeds and minimal power consumption of a few femtojoules per bit. These characteristics stem from the electrical switching of spontaneous polarization. Furthermore, in FTJ devices, written resistance states can be detected by measuring the junction conductance, eliminating the need for a destructive polarization switch. From the perspective of device applications, FTJs possess intriguing qualities. Unlike FE capacitors, where leakage currents negatively impact device performance, the conductance of FTJs serves as a functional characteristic. This unique property enables the utilization of FTJs in NVM devices that outperform current FeRAM.

Unlike FeRAM, where data is typically read out using the FE switching current, FTJs employ the tunneling current for data retrieval. However, FTJs face challenges such as limited on-off ratio and low read-out current. Band diagram engineering by inserting interfacial layers between metal and $Hf_xZr_{1-x}O_2$ has been reported in several works to improve the amount of read-out current. However, the thickness of these devices is still too thick to meet the requirement of read-out limitation of FTJ and degrade the polarization contribution due to the existence of an interfacial layer. By reducing the thickness of the FTJ, the transmission current can be largely modified. The FE polarization may strongly modulate the tunnel transmission, producing giant tunnel electroresistance (TER) with on/off ratios. Furthermore, different from classic planar FTJ, 3D stacking vertical FTJ has been reported with an excellent on/off ratio and endurance of 10^9 cycles which can be fabricated to high-density crossbar arrays.

34

4.2 DC and AC on/off Ratio of 6.7nm Superlattices

The MFM TiN $Hf_{0.5}Zr_{0.5}O_2$ TiN structure with O_2 exposure 30s is fabricated as an FTJ. The TEM image also defines the physical thickness of $Hf_{0.5}Zr_{0.5}O_2$, 6.7nm (Fig. 4.2-1(a)). According to our previous, the HAADF image (Fig. 4.2-1(b)) demonstrates clear ZrO_2-HfO_2 interfaces in the dark-bright fringes due to fewer $[V_o]$ resulting from long-time O_2 exposure. Meanwhile, good crystallinity of $Hf_{0.5}Zr_{0.5}O_2$ with 30s O_2 exposure is observed by TEM image. To achieve excellent ferroelectricity, wake-up is performed with a 4.5 MV/cm electrical field. High $2P_r=48\mu C/cm^2$ is obtained with $E_c=1.3MV/cm$. To extract the on-off ratio current, DC and AC measurements are applied in this chapter.
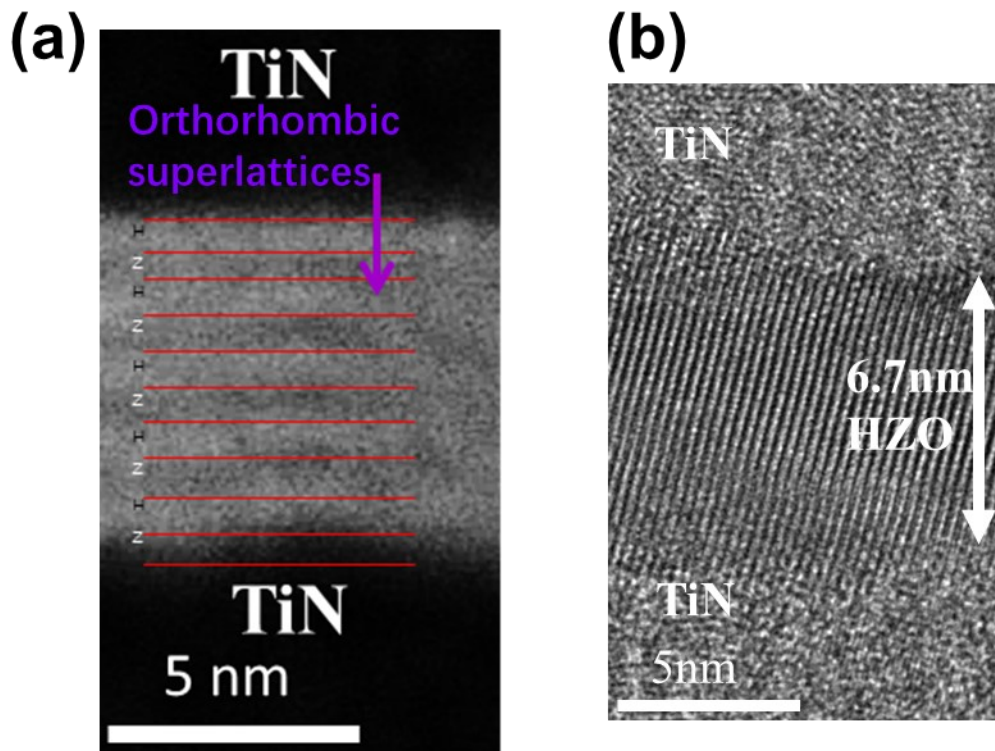
Fig. 4.2-1 (a) TEM and (b) HAADF images of $Hf_{0.5}Zr_{0.5}O_2$ with O_2 exposure 30s.

Fig. 4.2-2 P-E loop of 6.7nm superlattice $Hf_{0.5}Zr_{0.5}O_2$ with O_2 exposure 30s.

4.2.1 DC Measurement of 6.7nm Superlattices

The waveform of the DC sweep is shown in Fig. 4.2-3(a). To preset the direction of polarization, the sweeping voltage of -2 to 2V is applied initially in the sample. On current (J_{on}) appears after the opposite polarization switching, meaning a negative sweep (0 ~ -2V, 1st sweep) should follow the set positive polarization by -2 to 2V DC sweep. The measured J_{on} is shown as the dash in Fig. 4.2-3(b). Off current (J_{off}) appears when a negative sweep (0 ~ -2V, 2nd sweep) is followed with the set negative polarization by 2 to -2V DC sweep. The measured J_{off} is shown as the solid in Fig. On/off ratio of more than 100 achieved by the DC measurement in the superlattice $Hf_{0.5}Zr_{0.5}O_2$ with 30s O_2 exposure.

36

Fig. 4.2-3 (a) Waveform of DC measurement. (b) Swept on/off ratio of 6.7nm superlattice $Hf_{0.5}Zr_{0.5}O_2$ with O_2 exposure 30s.

4.2.2 AC Measurement of 6.7nm Superlattices

The waveform of AC pulse measurement is shown in Fig. 4.2-4(a). The preset pulse at the voltage of +3V/100ns is performed on the superlattice $Hf_{0.5}Zr_{0.5}O_2$ with 30s O_2 exposure. Pulse J_{on} occurs when applying the read pulse of -0.15V after a write pulse of +3V. With the increasing pulse width from 100ns to 10ms, the pulse on/off ratio increases to 68 (Fig. 4.2-4Fig. 4.2-3(b)). Note that the applying voltage of write is the same as that of PV measuring in Fig, and the read voltage of -0.15V is selected far less than V_c in Fig.

37

4.2-2.
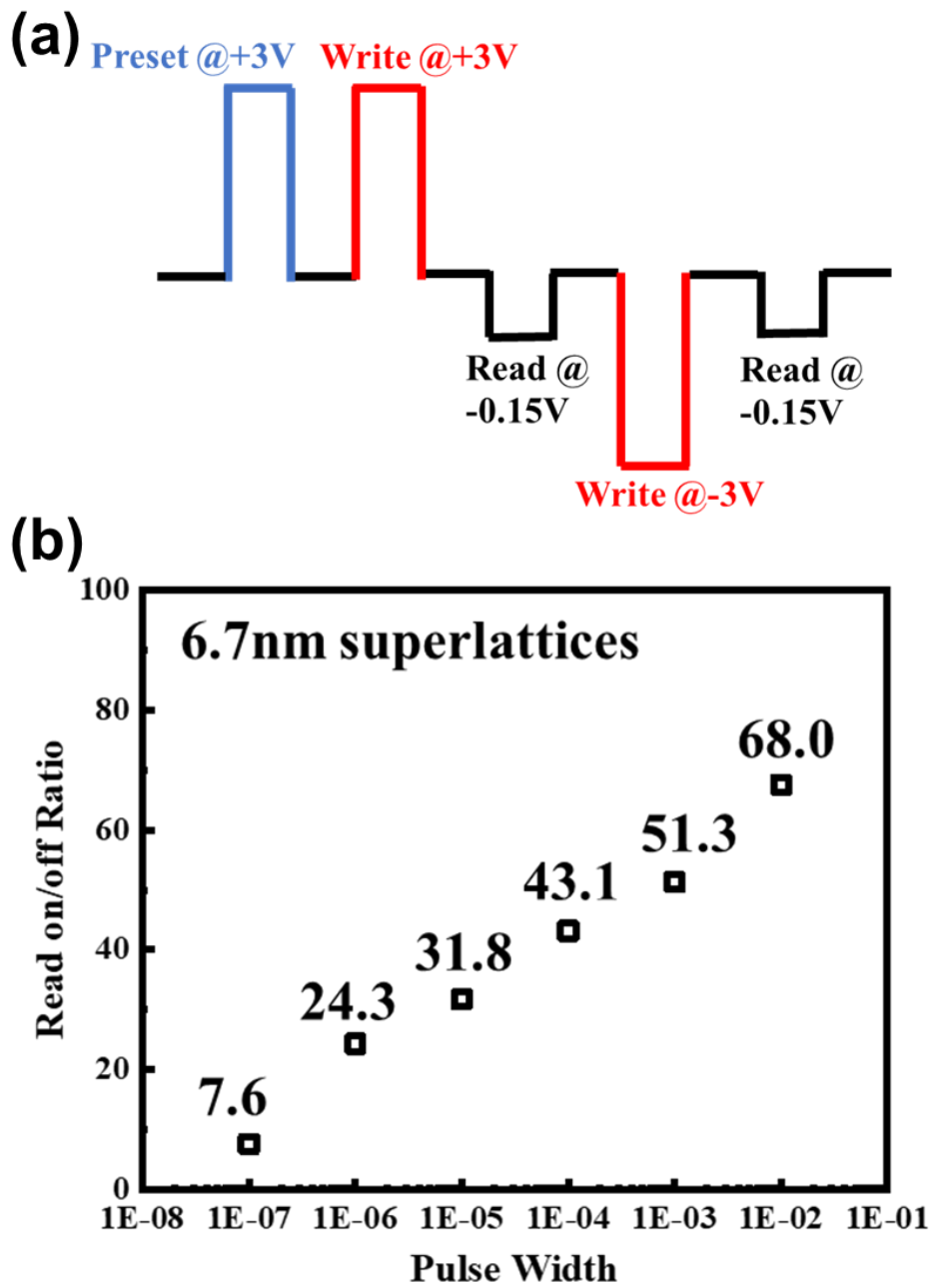
Fig. 4.2-4 (a) Waveform of AC measurement. (b) Pulse on/off ratio of 6.7nm superlattice $Hf_{0.5}Zr_{0.5}O_2$ with O_2 exposure 30s.

4.3 DC and AC on/off Ratio of 4nm Superlattices

Low read-out current has been considered one of the significant issues of FTJ

38

production. The total read-out current (switching current plus tunneling current) should be largely improved to increase the read-out current. Here we use the thinner thickness of superlattice $Hf_{0.5}Zr_{0.5}O_2$ with 30s O_2 exposure to enhance the tunneling current. By reducing the PEALD cycles of the HfO_2 and ZrO_2 mixture from 5 periods (6.7nm) to 3 periods (estimated 4nm), the MFM capacitor is fabricated for electrical analysis. Measured PV loop under 4.5MV/cm electrical field, same as the 6.7nm one, demonstrating excellent ferroelectricity with $2P_r=15\mu C/cm^2$ and $E_c=1.3MV/cm$ (Fig. 4.3-1). The V_c also decreases to 0.5V due to the thinner thickness. Besides, the C-V hysteresis shows two peaks in the forward and reverse C-V sweeps, indicating FE o-phase dominance. While decreasing the $Hf_{0.5}Zr_{0.5}O_2$ thickness, the grain size distribution is seriously affected[47]. O-phase population drops drastically with FE layer thickness reducing from 5nm to 2nm, and t-phase population keeps increasing with FE layer thickness decreasing[47]. It well explains the ferroelectricity loss with thinner $Hf_{0.5}Zr_{0.5}O_2$ thickness.
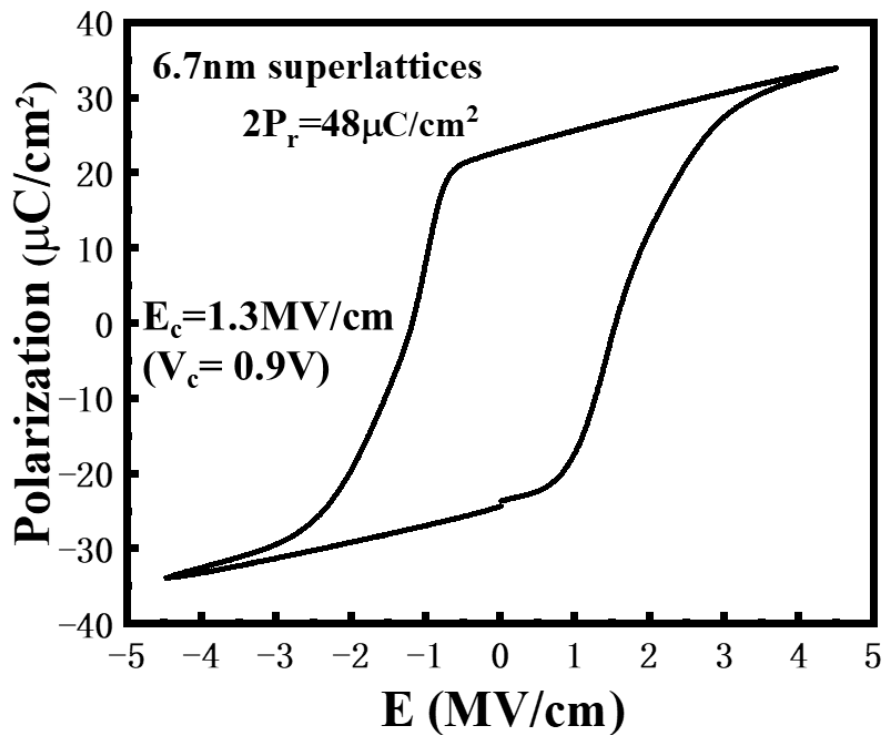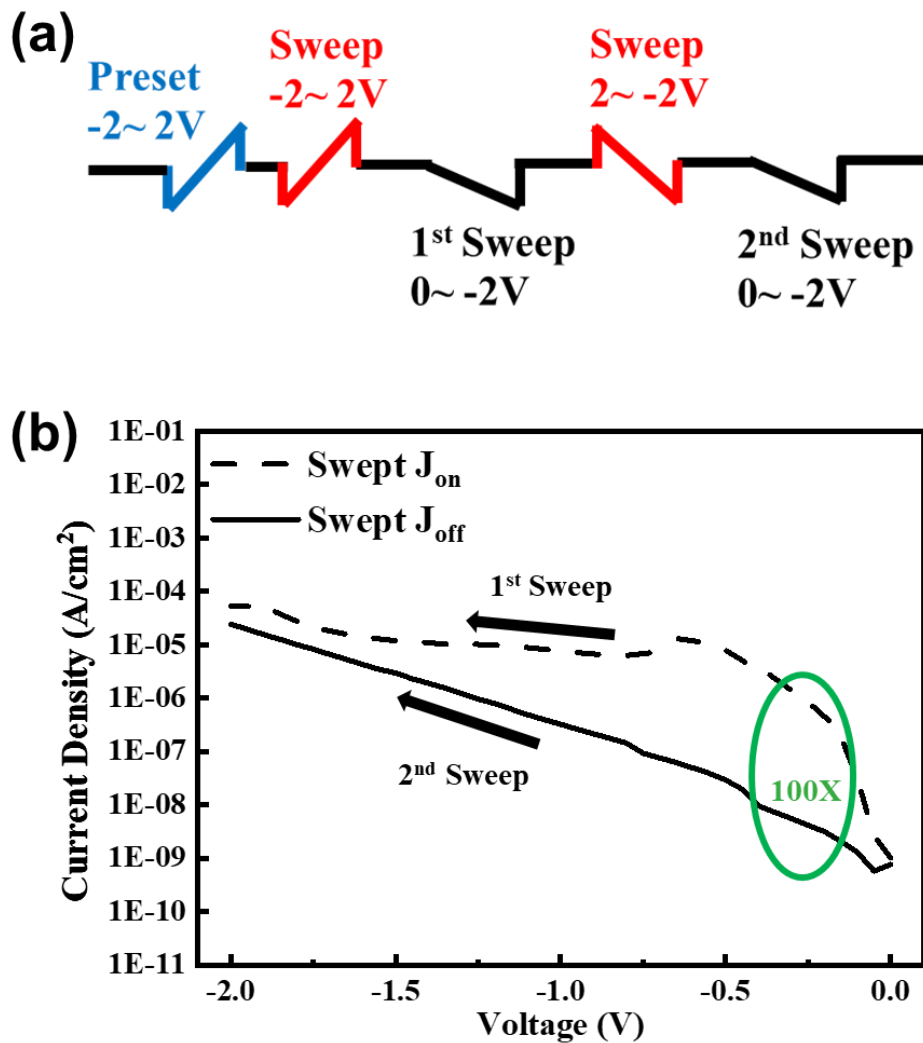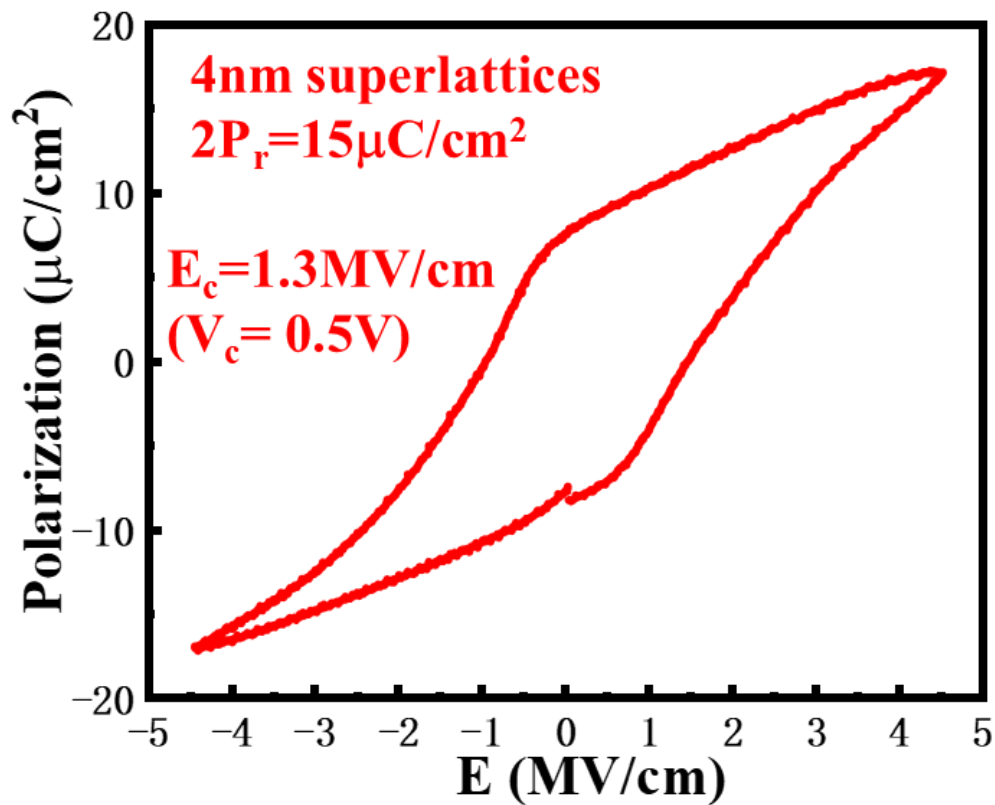
Fig. 4.3-1 P-E loop of 4nm superlattice $Hf_{0.5}Zr_{0.5}O_2$ with O_2 exposure 30s.

4.3.1 DC Measurement of 4nm Superlattices

The waveform of the DC sweep is shown as Fig. 4.2-3(a). The measured J_{on} of 4nm superlattice $Hf_{0.5}Zr_{0.5}O_2$ with 30s O_2 exposure is shown as the red dash in Fig. 4.3-2. The measured J_{off} as the red solid in Fig. 4.3-2. Swept J_{on} and J_{off} are separated clearly in 4nm superlattice $Hf_{0.5}Zr_{0.5}O_2$ with 30s O_2 exposure, and the on/off ratio is more than 10. Compared with the on/off ratio of 6.7nm MFM, the decrease could be the reason for ferroelectricity loss. However, the amount of tunneling current is improved by more than 1000 and meets the expectation.
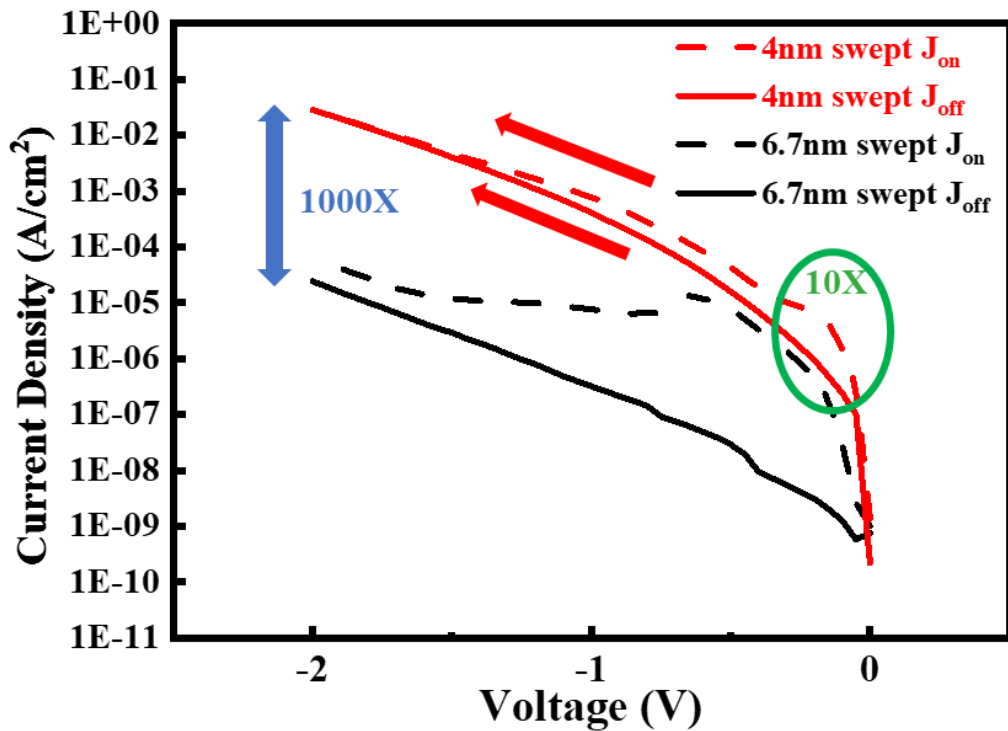
Fig. 4.3-2 Swept on/off ratio of 4nm $Hf_{0.5}Zr_{0.5}O_2$ vs. 6.7nm $Hf_{0.5}Zr_{0.5}O_2$.

4.3.2 AC Measurement of 4nm Superlattices

The waveform of AC pulse measurement is shown in Fig. 4.3-3(a). The preset pulse at the voltage of +1.8V/100ns is consistently performed on the 4nm superlattice $Hf_{0.5}Zr_{0.5}O_2$ with 30s O_2 exposure. The measured on/off ratio of 4nm MFM increases from 1.4 to 2.1 with the pulse width increasing from 100ns to 10ms, shown in Fig. 4.3-3(b). Read on/off ratio of 4nm FTJ saturates at 2.1 after the pulse width increases to 1ms. Due to the surge of tunneling current, the on/off ratio is lower than that on 6.7nm FTJ. Note that the applying voltage of write is the same as that of PV measuring in Fig. 4.3-1 to maintain the V_c and the read voltage of -0.15V is selected far less than V_c in Fig. 4.3-1.
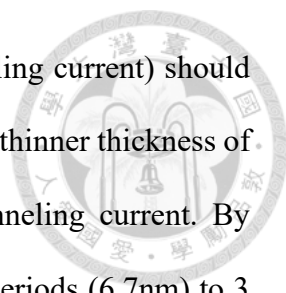
41
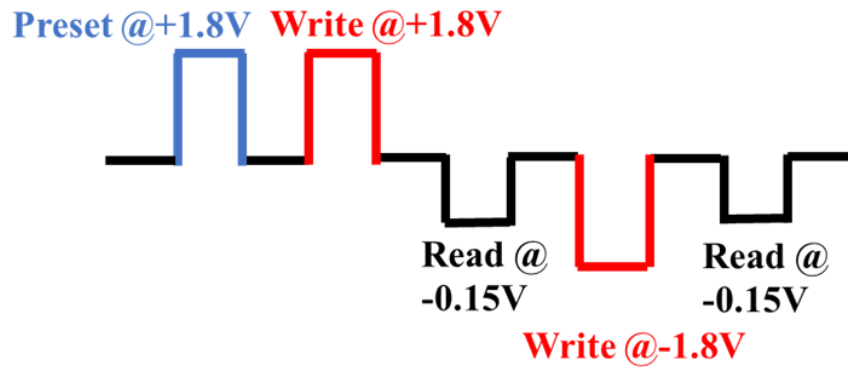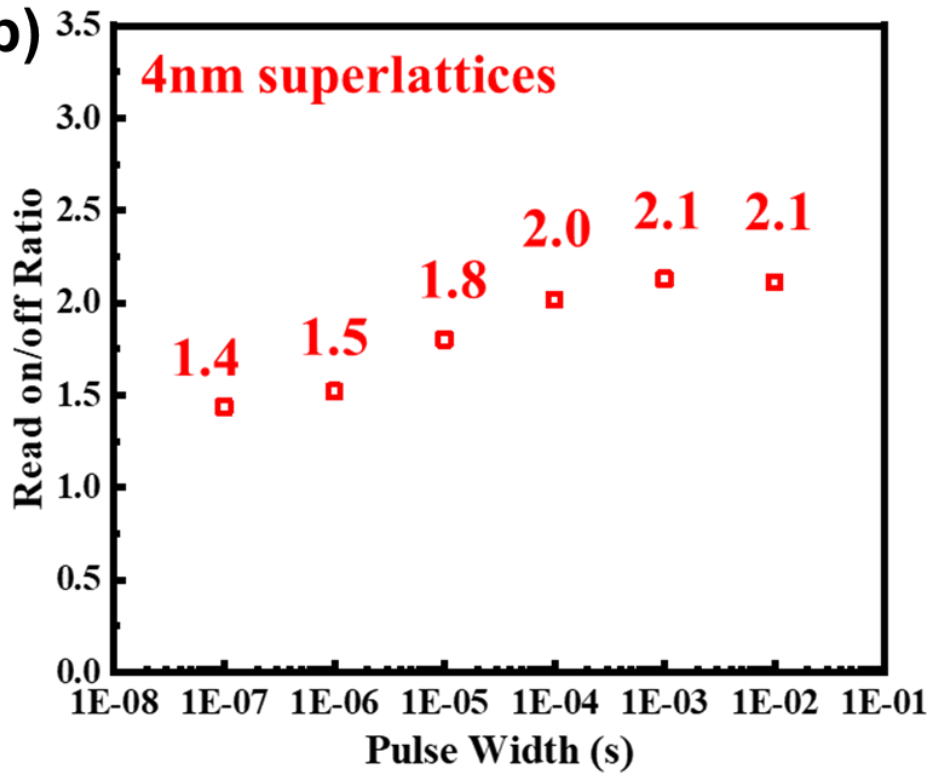
Fig. 4.3-3 Waveform of AC measurement. (b) Pulse on/off ratio of 4nm superlattice $Hf_{0.5}Zr_{0.5}O_2$ with O_2 exposure 30s.

4.4 Summary

The thickness effect is investigated in this chapter. To solve the problem of a small read-out current, the HZO thickness is decreased from 6.7nm to 4nm. On 6.7nm superlattice $Hf_{0.5}Zr_{0.5}O_2$ with 30s O_2 exposure, the DC on/off ratio is more than 100 while

the AC on/off ratio is 67.8 at -0.15V with a 10ms read pulse. On 4nm superlattice Hf$_{0.5}$Zr$_{0.5}$O$_2$ with 30s O$_2$ exposure, the DC on/off ratio is more than 10 while the AC on/off ratio is 2.1 at -0.15V with a 10ms read pulse.
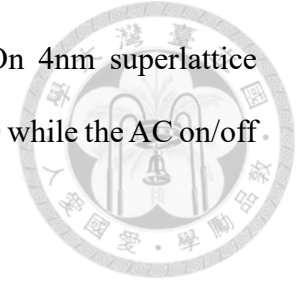
Chapter 5 - Summary and Future Work

5.1 Summary

The experimental and theoretical analysis considering [V_o], cryogenic phase transition, and thickness effect of $Hf_{0.5}Zr_{0.5}O_2$ are studied in this thesis. PEALD fabricates the MFM capacitor to ensure the high-quality $Hf_{0.5}Zr_{0.5}O_2$ thin film. The material analysis and electrical properties are investigated. Also, various measurement temperature is performed in superlattice and alloy structures to verify the cryogenic phase transition. LDG fitting and first-principle calculation are combined to demonstrate the origin of cryogenic phase transition. To improve the read-out current, the thickness of $Hf_{0.5}Zr_{0.5}O_2$ is reduced by decreasing PEALD cycles. DC and AC measurements are applied to investigate the on/off ratio.

In Chapter 2, $Hf_{0.5}Zr_{0.5}O_2$ with O_2 exposure 5s and 10s are fabricated by PEALD. By tuning the O_2 exposure time in film growth, [V_o] of material is controlled. TEM and HAADF images characterize the PEALD layer while high [V_o] favors AFE t-phase and low [V_o] favors FE o-phase. Electrical analysis, including C-V, P-V, and dielectric constant, are also consistent with the conclusion.

Chapter 3's calculations based on the relative free energies and energy barriers provide insights into enhancing FE properties through the t- to o-phase transition in $Hf_{0.5}Zr_{0.5}O_2$ with decreasing temperature. The decrease in the energy barrier facilitates the transformation to the o-phase, resulting in improved FE behavior, as observed in the experimental data.

In Chapter 4, the read-out current is efficiently enhanced by decreasing the thickness of $Hf_{0.5}Zr_{0.5}O_2$. Compared with the DC and AC measurement of thicker and thinner FE layers, on/off ratio undergoes a decrease in the thinner one due to the rapid increase of

44

tunneling current. By benchmarking our data and other works, the 4nm $Hf_{0.5}Zr_{0.5}O_2$ demonstrate excellent FE properties beyond 5nm.
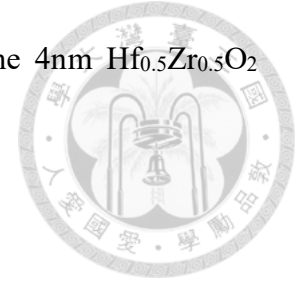
5.2 Future Work

1. Fabrication of ultrathin $Hf_{0.5}Zr_{0.5}O_2$ with high crystallinity film.

2. Performance improvement of ultrathin $Hf_{0.5}Zr_{0.5}O_2$.

3. Band engineering by adding an interfacial layer.

4. Investigating the strain effect of $Hf_{0.5}Zr_{0.5}O_2$.

5. FeFET with a high proportion of FE o-phase.

5.3 Reference

[1] P. Cappelletti, "Non volatile memory evolution and revolution," in *2015 IEEE International Electron Devices Meeting (IEDM)*, 2015: IEEE, pp. 10.1. 1-10.1. 4.

[2] P. Jain, U. Arslan, M. Sekhar, B. C. Lin, L. Wei, T. Sahu, J. Alzate-Vinasco, A. Vangapaty, M. Meterelliyoz, and N. Strutt, "13.2 A 3.6 Mb 10.1 Mb/mm^2 embedded non-volatile ReRAM macro in 22nm FinFET technology with adaptive forming/set/reset schemes yielding down to 0.5 V with sensing time of 5ns at 0.7 V," in *2019 IEEE International Solid-State Circuits Conference-(ISSCC)*, 2019: IEEE, pp. 212-214.

[3] J. Wu, Y. Chen, W. Khwa, S. Yu, T. Wang, J. Tseng, Y. Chih, and C. H. Diaz, "A 40nm low-power logic compatible phase change memory technology," in *2018 IEEE International Electron Devices Meeting (IEDM)*, 2018: IEEE, pp. 27.6. 1-27.6. 4.

[4] Y.-D. Chih, Y.-C. Shih, C.-F. Lee, Y.-A. Chang, P.-H. Lee, H.-J. Lin, Y.-L. Chen, C.-P. Lo, M.-C. Shih, and K.-H. Shen, "13.3 a 22nm 32mb embedded stt-mram with 10ns read speed, 1m cycle write endurance, 10 years retention at 150 c and high immunity to

magnetic field interference," in *2020 IEEE International Solid-State Circuits Conference-(ISSCC)*, 2020: IEEE, pp. 222-224.

[5]   M. Trentzsch, S. Flachowsky, R. Richter, J. Paul, B. Reimer, D. Utess, S. Jansen, H. Mulaosmanovic, S. Müller, and S. Slesazeck, "A 28nm HKMG super low power embedded NVM technology based on ferroelectric FETs," in *2016 IEEE International Electron Devices Meeting (IEDM)*, 2016: IEEE, pp. 11.5. 1-11.5. 4.

[6]   Y. Kwon and M. Rhu, "Beyond the memory wall: A case for memory-centric hpc system for deep learning," in *2018 51st Annual IEEE/ACM International Symposium on Microarchitecture (MICRO)*, 2018: IEEE, pp. 148-161.

[7]   K. Lee, J. J. Kan, and S. H. Kang, "Unified embedded non-volatile memory for emerging mobile markets," in *Proceedings of the 2014 international symposium on Low power electronics and design*, 2014, pp. 131-136.

[8]   Q. Luo, T. Gong, Y. Cheng, Q. Zhang, H. Yu, J. Yu, H. Ma, X. Xu, K. Huang, and X. Zhu, "Hybrid 1T e-DRAM and e-NVM realized in one 10 nm node ferro FinFET device with charge trapping and domain switching effects," in *2018 IEEE International Electron Devices Meeting (IEDM)*, 2018: IEEE, pp. 2.6. 1-2.6. 4.

[9]   S.-C. Chang, N. Haratipour, S. Shivaraman, C. Neumann, S. Atanasov, J. Peck, N. Kabir, I.-C. Tung, H. Liu, and B. Krist, "FeRAM using anti-ferroelectric capacitors for high-speed and high-density embedded memory," in *2021 IEEE International Electron Devices Meeting (IEDM)*, 2021: IEEE, pp. 33.2. 1-33.2. 4.

[10] J.-Y. Lee, F.-S. Chang, K.-Y. Hsiang, P.-H. Chen, Z.-F. Luo, Z.-X. Li, J.-H. Tsai, C. W. Liu, and M. H. Lee, "3D Stackable Vertical Ferroelectric Tunneling Junction (V-FTJ) with on/off Ratio 1500x, Applicable Cell Current, Self-Rectifying Ratio 1000x, Robust Endurance of 10^9 Cycles, Multilevel and Demonstrated Macro Operation Toward High-Density BEOL NVMs," in *2023 IEEE Symposium on VLSI Technology and Circuits (VLSI*

Technology and Circuits), 2023.

[11] Y.-R. Chen, Y.-C. Liu, Z. Zhao, W.-H. Hsieh, J.-Y. Lee, C.-T. Tu, B.-W. Huang, J.-F. Wang, S.-J. Chueh, Y. Xing, G.-H. Chen, H.-C. Chou, D. S. Woo, M. H. Lee, and C. Liu, "First Stacked Nanosheet FeFET Featuring Memory Window of 1.8V at Record Low Write Voltage of 2V and Endurance >1E11 Cycles," in *2023 IEEE Symposium on VLSI Technology and Circuits (VLSI Technology and Circuits)*, 2023.

[12] J. Muller, T. S. Boscke, U. Schroder, S. Mueller, D. Brauhaus, U. Bottger, L. Frey, and T. Mikolajick, "Ferroelectricity in simple binary ZrO_2 and HfO_2," *Nano letters,* vol. 12, no. 8, pp. 4318-4323, 2012.

[13] T. Francois, L. Grenouillet, J. Coignus, P. Blaise, C. Carabasse, N. Vaxelaire, T. Magis, F. Aussenac, V. Loup, and C. Pellissier, "Demonstration of BEOL-compatible ferroelectric $Hf_{0.5} Zr_{0.5} O_2$ scaled FeRAM co-integrated with 130nm CMOS for embedded NVM applications," in *2019 IEEE International Electron Devices Meeting (IEDM)*, 2019: IEEE, pp. 15.7. 1-15.7. 4.

[14] Y. Goh and S. Jeon, "The effect of the bottom electrode on ferroelectric tunnel junctions based on CMOS-compatible HfO_2," *Nanotechnology,* vol. 29, no. 33, p. 335201, 2018.

[15] S.-H. Kuk, S.-M. Han, B.-H. Kim, S.-H. Baek, J.-H. Han, and S.-h. Kim, "Comprehensive understanding of the HZO-based n/pFeFET operation and device performance enhancement strategy," in *2021 IEEE International Electron Devices Meeting (IEDM)*, 2021: IEEE, pp. 33.6. 1-33.6. 4.

[16] Q. Luo, Y. Cheng, J. Yang, R. Cao, H. Ma, Y. Yang, R. Huang, W. Wei, Y. Zheng, and T. Gong, "A highly CMOS compatible hafnia-based ferroelectric diode," *Nature communications,* vol. 11, no. 1, p. 1391, 2020.

[17] J. Hur, Y.-C. Luo, Z. Wang, S. Lombardo, A. I. Khan, and S. Yu, "Characterizing

47

doi:10.6342/NTU202301680

ferroelectric properties of $Hf_{0.5}Zr_{0.5}O_2$ from deep-cryogenic temperature (4 K) to 400 k," *IEEE Journal on Exploratory Solid-State Computational Devices and Circuits,* vol. 7, no. 2, pp. 168-174, 2021.

[18] Y.-R. Chen, Z. Zhao, C.-T. Tu, Y.-C. Liu, B.-W. Huang, Y. Xing, G.-H. Chen, and C. Liu, "I_{ON} Enhancement of $Ge_{0.98}Si_{0.02}$ Nanowire nFETs by High-κ Dielectrics," *IEEE Electron Device Letters,* vol. 43, no. 10, pp. 1601-1604, 2022.

[19] T. Mimura, T. Shimizu, O. Sakata, and H. Funakubo, "Large thermal hysteresis of ferroelectric transition in HfO_2-based ferroelectric films," *Applied Physics Letters,* vol. 118, no. 11, p. 112903, 2021.

[20] M. H. Park, Y. H. Lee, T. Mikolajick, U. Schroeder, and C. S. Hwang, "Thermodynamic and kinetic origins of ferroelectricity in fluorite structure oxides," *Advanced Electronic Materials,* vol. 5, no. 3, p. 1800522, 2019.

[21] T. Xin, Y. Zheng, Y. Cheng, K. Du, Y. Wang, Z. Gao, D. Su, Y. Zheng, Q. Zhong, and C. Liu, "Atomic visualization of the emergence of orthorhombic phase in $Hf_{0.5}Zr_{0.5}O_2$ ferroelectric film with in-situ rapid thermal annealing," in *2022 IEEE Symposium on VLSI Technology and Circuits (VLSI Technology and Circuits)*, 2022: IEEE, pp. 343-344.

[22] K. Ni, A. Saha, W. Chakraborty, H. Ye, B. Grisafe, J. Smith, G. B. Rayner, S. Gupta, and S. Datta, "Equivalent oxide thickness (EOT) scaling with hafnium zirconium oxide high-κ dielectric near morphotropic phase boundary," in *2019 IEEE international electron devices meeting (IEDM)*, 2019: IEEE, pp. 7.4. 1-7.4. 4.

[23] R. Materlik, C. Künneth, and A. Kersch, "The origin of ferroelectricity in $Hf_{1-x}Zr_xO_2$: A computational investigation and a surface energy model," *Journal of Applied Physics,* vol. 117, no. 13, p. 134109, 2015.

[24] Z. Zhao, Y.-R. Chen, J.-F. Wang, Y.-W. Chen, J.-R. Zou, Y. Lin, Y. Xing, C. Liu, and C. Hu, "Engineering $Hf_{0.5}Zr_{0.5}O_2$ ferroelectric/anti-ferroelectric phases with oxygen

vacancy and interface energy achieving high remanent polarization and dielectric constants," *IEEE Electron Device Letters,* vol. 43, no. 4, pp. 553-556, 2022.

[25] D. Gupta, V. Chauhan, and R. Kumar, "A comprehensive review on synthesis and applications of molybdenum disulfide (MoS_2) material: Past and recent developments," *Inorganic Chemistry Communications,* vol. 121, p. 108200, 2020.

[26] Y.-K. Liang, J.-S. Wu, C.-Y. Teng, H.-L. Ko, Q.-H. Luc, C.-J. Su, E.-Y. Chang, and C.-H. Lin, "Demonstration of Highly Robust 5 nm $Hf_{0.5}Zr_{0.5}O_2$ Ultra-Thin Ferroelectric Capacitor by Improving Interface Quality," *IEEE Electron Device Letters,* vol. 42, no. 9, pp. 1299-1302, 2021.

[27] L. Baumgarten, T. Szyjka, T. Mittmann, M. Materano, Y. Matveyev, C. Schlueter, T. Mikolajick, U. Schroeder, and M. Müller, "Impact of vacancies and impurities on ferroelectricity in PVD-and ALD-grown HfO_2 films," *Applied Physics Letters,* vol. 118, no. 3, p. 032903, 2021.

[28] M. Martínez-Puente, P. Horley, F. Aguirre-Tostado, J. López-Medina, H. Borbón-Nuñez, H. Tiznado, A. Susarrey-Arce, and E. Martínez-Guerra, "ALD and PEALD deposition of HfO_2 and its effects on the nature of oxygen vacancies," *Materials Science and Engineering: B,* vol. 285, p. 115964, 2022.

[29] Y.-J. Lin, C.-Y. Teng, C. Hu, C.-J. Su, and Y.-C. Tseng, "Impacts of surface nitridation on crystalline ferroelectric phase of $Hf_{1-x}Zr_xO_2$ and ferroelectric FET performance," *Applied Physics Letters,* vol. 119, no. 19, p. 192102, 2021.

[30] M. Hyuk Park, H. Joon Kim, Y. Jin Kim, W. Lee, H. Kyeom Kim, and C. Seong Hwang, "Effect of forming gas annealing on the ferroelectric properties of $Hf_{0.5}Zr_{0.5}O_2$ thin films with and without Pt electrodes," *Applied Physics Letters,* vol. 102, no. 11, p. 112914, 2013.

[31] S. J. Kim, J. Mohan, H. S. Kim, J. Lee, S. M. Hwang, D. Narayan, J.-G. Lee, C. D.

Young, L. Colombo, and G. Goodman, "Effect of hydrogen derived from oxygen source on low-temperature ferroelectric TiN/Hf$_{0.5}$Zr$_{0.5}$O$_2$/TiN capacitors," *Applied Physics Letters,* vol. 115, no. 18, p. 182901, 2019.
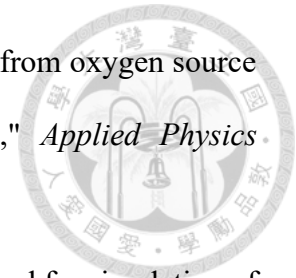
[32] A. Rosenauer and M. Schowalter, "STEMSIM-a new software tool for simulation of STEM HAADF Z-contrast imaging," *Springer Proceedings in Physics,* vol. 120, pp. 169-172, 2008.

[33] X. Zhao and D. Vanderbilt, "First-principles study of structural, vibrational, and lattice dielectric properties of hafnium oxide," *Physical Review B,* vol. 65, no. 23, p. 233106, 2002.
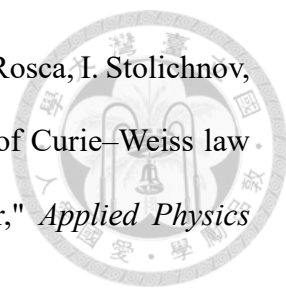
[34] D. Vanderbilt, X. Zhao, and D. Ceresoli, "Structural and dielectric properties of crystalline and amorphous ZrO$_2$," *Thin Solid Films,* vol. 486, no. 1-2, pp. 125-128, 2005.

[35] C. Künneth, R. Materlik, and A. Kersch, "Modeling ferroelectric film properties and size effects from tetragonal interlayer in Hf$_{1-x}$Zr$_x$O$_2$ grains," *Journal of Applied Physics,* vol. 121, no. 20, p. 205304, 2017.

[36] S. S. Cheema, N. Shanker, L.-C. Wang, C.-H. Hsu, S.-L. Hsu, Y.-H. Liao, M. San Jose, J. Gomez, W. Chakraborty, and W. Li, "Ultrathin ferroic HfO$_2$–ZrO$_2$ superlattice gate stack for advanced transistors," *Nature,* vol. 604, no. 7904, pp. 65-71, 2022.

[37] U. Schroeder, T. Mittmann, M. Materano, P. D. Lomenzo, P. Edgington, Y. H. Lee, M. Alotaibi, A. R. West, T. Mikolajick, and A. Kersch, "Temperature-Dependent Phase Transitions in Hf$_x$Zr$_{1-x}$O$_2$ Mixed Oxides: Indications of a Proper Ferroelectric Material," *Advanced Electronic Materials,* vol. 8, no. 9, p. 2200265, 2022.

[38] Y. Zhang, Z. Fan, D. Wang, J. Wang, Z. Zou, Y. Li, Q. Li, R. Tao, D. Chen, and M. Zeng, "Enhanced Ferroelectric Properties and Insulator–Metal Transition-Induced Shift of Polarization-Voltage Hysteresis Loop in VO x-Capped Hf$_{0.5}$Zr$_{0.5}$O$_2$ Thin Films," *ACS Applied Materials & Interfaces,* vol. 12, no. 36, pp. 40510-40517, 2020.

[39] C. Gastaldi, M. Cavalieri, A. Saeidi, E. O'Connor, S. Kamaei, T. Rosca, I. Stolichnov, and A. M. Ionescu, "Intrinsic switching in Si-doped HfO_2: A study of Curie–Weiss law and its implications for negative capacitance field-effect transistor," *Applied Physics Letters,* vol. 118, no. 19, p. 192904, 2021.

[40] P. D. Lomenzo, S. Jachalke, H. Stoecker, E. Mehner, C. Richter, T. Mikolajick, and U. Schroeder, "Universal Curie constant and pyroelectricity in doped ferroelectric HfO_2 thin films," *Nano Energy,* vol. 74, p. 104733, 2020.

[41] T. Shimizu, K. Katayama, T. Kiguchi, A. Akama, T. J. Konno, O. Sakata, and H. Funakubo, "The demonstration of significant ferroelectricity in epitaxial Y-doped HfO_2 film," *Scientific reports,* vol. 6, no. 1, p. 32931, 2016.

[42] H. Chen, L. Tang, L. Liu, Y. Chen, H. Luo, X. Yuan, and D. Zhang, "Temperature dependent polarization-switching behavior in $Hf_{0.5}Zr_{0.5}O_2$ ferroelectric film," *Materialia,* vol. 14, p. 100919, 2020.

[43] T. Mittmann, M. Materano, S.-C. Chang, I. Karpov, T. Mikolajick, and U. Schroeder, "Impact of oxygen vacancy content in ferroelectric HZO films on the device performance," in *2020 IEEE International Electron Devices Meeting (IEDM)*, 2020: IEEE, pp. 18.4. 1-18.4. 4.

[44] Z. Fan, J. Chen, and J. Wang, "Ferroelectric HfO_2-based materials for next-generation ferroelectric memories," *Journal of Advanced Dielectrics,* vol. 6, no. 02, p. 1630003, 2016.

[45] H. Mulaosmanovic, E. T. Breyer, T. Mikolajick, and S. Slesazeck, "Ferroelectric FETs with 20-nm-thick HfO_2 layer for large memory window and high performance," *IEEE Transactions on Electron Devices,* vol. 66, no. 9, pp. 3828-3833, 2019.

[46] Y.-T. Tang, C.-J. Su, Y.-S. Wang, K.-H. Kao, T.-L. Wu, P.-J. Sung, F.-J. Hou, C.-J. Wang, M.-S. Yeh, and Y.-J. Lee, "A comprehensive study of polymorphic phase

distribution of ferroelectric-dielectrics and interfacial layer effects on negative capacitance FETs for sub-5 nm node," in *2018 IEEE Symposium on VLSI Technology*, 2018: IEEE, pp. 45-46.

[47] Y.-W. Chen and C. Liu, "Boost of orthorhombic population with amorphous SiO_2 interfacial layer—a DFT study," *Semiconductor Science and Technology,* vol. 37, no. 5, p. 05LT01, 2022.

[48] H. J. Kim, M. H. Park, Y. J. Kim, Y. H. Lee, W. Jeon, T. Gwon, T. Moon, K. D. Kim, and C. S. Hwang, "Grain size engineering for ferroelectric $Hf_{0.5}Zr_{0.5}O_2$ films by an insertion of Al_2O_3 interlayer," *Applied Physics Letters,* vol. 105, no. 19, p. 192903, 2014.

[49] J. Wu, F. Mo, T. Saraya, T. Hiramoto, and M. Kobayashi, "A first-principles study on ferroelectric phase formation of Si-doped HfO_2 through nucleation and phase transition in thermal process," *Applied Physics Letters,* vol. 117, no. 25, p. 252904, 2020.

[50] B. M. Hudak, S. W. Depner, G. R. Waetzig, A. Talapatra, R. Arroyave, S. Banerjee, and B. S. Guiton, "Real-time atomistic observation of structural phase transformations in individual hafnia nanorods," *Nature communications,* vol. 8, no. 1, p. 15316, 2017.

[51] A. Toriumi, Y. Nakajima, and K. Kita, "Opportunity for Phase-Controlled Higher-k HfO2," *ECS Transactions,* vol. 41, no. 7, p. 125, 2011.

[52] Y. H. Lee, S. D. Hyun, H. J. Kim, J. S. Kim, C. Yoo, T. Moon, K. D. Kim, H. W. Park, Y. B. Lee, and B. S. Kim, "Nucleation-limited ferroelectric orthorhombic phase formation in $Hf_{0.5}Zr_{0.5}O_2$ thin films," *Advanced Electronic Materials,* vol. 5, no. 2, p. 1800436, 2019.

[53] A. Kashir, H. Kim, S. Oh, and H. Hwang, "Large remnant polarization in a wake-up free $Hf_{0.5}Zr_{0.5}O_2$ ferroelectric film through bulk and interface engineering," *ACS Applied Electronic Materials,* vol. 3, no. 2, pp. 629-638, 2021.

[54] S. E. Reyes-Lillo, K. F. Garrity, and K. M. Rabe, "Antiferroelectricity in thin-film

ZrO$_2$ from first principles," *Physical Review B,* vol. 90, no. 14, p. 140103, 2014.

[55] T. D. Huan, V. Sharma, G. A. Rossetti Jr, and R. Ramprasad, "Pathways towards ferroelectricity in hafnia," *Physical Review B,* vol. 90, no. 6, p. 064111, 2014.

[56] S.-J. Chang, C.-Y. Teng, Y.-J. Lin, T.-M. Wu, M.-H. Lee, B.-H. Lin, M.-T. Tang, T.-S. Wu, C. Hu, and E. Y.-T. Tang, "Visualizing Ferroelectric Uniformity of Hf1−x Zr x O2 Films Using X-ray Mapping," *ACS Applied Materials & Interfaces,* vol. 13, no. 24, pp. 29212-29221, 2021.

[57] J. Adkins, I. Fina, F. Sánchez, S. Bakaul, and J. Abiade, "Thermal evolution of ferroelectric behavior in epitaxial Hf$_{0.5}$Zr$_{0.5}$O$_2$," *Applied Physics Letters,* vol. 117, no. 14, p. 142902, 2020.